POLITECNICO DI TORINO

Master's Degree in Environmental and Land Engineering
Climate Change

Master's Thesis

GIS-based Assessment of Pluvial Flooding Using the SCS-CN Method and High-Resolution LiDAR Data: A Case Study of Turin, Italy

Supervisors

Prof. Piero Boccardo
Prof. Alberto Viglione

Candidate

Fatima Baha Eddine

Academic Year 2025/2026

Abstract

Rapid urbanization and population growth are leading to an increased flood risk in urban areas, related to a combination of meteorological and hydrological factors, as well as land-use changes and inadequate flood defense infrastructures. This study analyzed the impact of precipitation on surface runoff generation, using the Soil Conservation Service Curve Number (SCS-CN) hydrological model coupled with high-resolution Light Detection and Ranging (LiDAR) data. The study area of approximately 2 km^2 is located in the northeastern part of Turin, in the Piedmont region of Italy. Precipitation scenarios were defined based on Intensity-Duration-Frequency (IDF) curves, considering return periods of 5, 10, 20, and 50 years, and rainfall event durations of 1, 3, and 6 hours. The curves were obtained using the daily rainfall time series over the period 1994-2024, retrieved from the Regional Environmental Protection Agency (ARPA) Piedmont catalog. Flood vulnerability maps were generated to visualize the drainage system criticality at a sub-basin scale, comparing surface runoff against the estimated conveyance capacity of the network. The analysis considered two inlet clogging scenarios: 0% (unobstructed) and 50% (partially obstructed). Future climate scenarios (IPCC CMIP5 RCP 4.5 and RCP 8.5) over the period 2026–2070 were analyzed and bias-corrected via the Quantile Mapping (QM) method. The dataset was derived from the COSMO-CLM regional climate model at a spatial resolution of 8 km, resulting from a downscaling process over Italy performed by the Climate Limited-area Modelling (CLM) Community. Ultimately, a Python-based workflow was developed to visualize the accumulated water within a 3D scene of the study area.

Table of Contents

List of Tables

List of Figures

Glossary

AMC
Antecedent Moisture Condition

AMS
Annual Maxima Series

ARPA
Agenzia Regionale per la Protezione Ambientale

ASPRS
American Society of Photogrammetry and Remote Sensing

CLM
Climate Limited-area Modelling

CN
Curve Number

CTC
Carta Tecnica Comunale

DSM
Digital Surface Model

DTM
Digital Terrain Model

DN
Digital Number

EVI
Extreme Value Type I

GIS

Geographic Information Systems

HSG

Hydrological Soil Group

IDF

Intensity-Duration-Frequency

LiDAR

Light Detection and Ranging

MAE

Mean Absolute Error

MLC

Maximum Likelihood Classification

NBS

Nature-Based Solutions

NRCS

Natural Resources Conservation Service

NSE

Nash-Sutcliffe Efficiency

NSSDA

National Standard for Spatial Data Accuracy

QM

Quantile Mapping

RCM

Regional Climate Model

RCP

Representative Concentration Pathways

RMSE

Root Mean Square Error

ROI

Region of Interest

RS

Remote Sensing

SCS-CN

Soil Conservation Service Curve Number

SMAT

Società Metropolitana Acque Torino S.p.A.

SUDS

Sustainable Urban Drainage Systems

USDA

U.S. Department of Agriculture

Chapter 1

Introduction

On a global scale, floods represent the most common disruptive natural events, concerning both rural and urban environments. As a consequence of urbanization and population growth, floods are affecting an increasing number of urban areas, typically due to multiple factors, particularly meteorological and hydrological extremes. Increasing flood risk is primarily attributable to a lack of flood defense measures as well as land use changes, leading to lower soil permeability and higher surface runoff. An example of a typical flooding driver can be high-intensity rainfall in cases when drainage systems do not have the needed capacity to cope with runoffs. Another analogous case occurs when water enters the sewage system at one point and emerges at others. Another potential factor to have a significant impact on the increasing flood risk is climate change, more specifically, meteorological pattern alteration associated with a warmer climate. Nevertheless, at present, it has been assessed that shorter timescales, natural variability, and other non-climatic risks are more impactful on flood risk, as accelerating urbanization is an example. [1] With the aim of adapting and mitigating flooding risks, a proper management framework for urban flooding is needed. Particularly, remote sensing techniques act as an important support in disaster management strategies, as in the case of sudden urban flood hazards. Geographic Information Systems (GIS) and remote sensing (RS) are considered valid tools used in the evaluation and management of urban watershed properties. Indeed, when combined with hydrological models, these systems can significantly improve the accuracy and reliability with respect to traditional methods. An example of a widely adopted technique is the Soil Conservation Service Curve Number (SCS-CN) method, designed by the Natural Resources Conservation Service (NRCS) of the U.S. Department of Agriculture (USDA). This method is commonly used in hydrological studies to evaluate surface runoff by integrating multiple factors—such as soil type, land use, and topography—into a single value, also called the Curve Number (CN) parameter. Recently, a GIS-based implementation of the SCS–CN method has become a widespread approach in the assessment of hydrological impacts of land use changes and urban expansion, especially in

regions characterized by a lack of available data. The result consists of a spatial distribution of superficial runoff, which makes this method cost-effective and a relatively straightforward solution to address watershed modeling [2]. In this study, the SCS–CN method is implemented within a GIS environment to evaluate the effects of urban land use and to analyze the spatial variability of surface runoff in the presence of an intense rainfall event.

Chapter 2

Materials and Methods

2.1 Study Area

The city of Turin is situated in the north-west of Italy within the Piedmont region. Placed in the Po Valley and surrounded by the western Alps and Superga Hill, Turin lies on a terraced fluvial plain at an orthometric height of 275–210 m, with an urban area spreading over a relatively flat terrain, while the surrounding hills reach elevations up to 715 m. The city embraces an area of about 130.2 km^2 and is crossed by the largest Italian river (Po river) and its three main tributaries (the Sangone, Dora Riparia, and Stura di Lanzo rivers). The geological composition of Turin is characterized by Holocene alluvial deposits overlaying Cenozoic marine sediments, particularly evident in the Turin Hill area. These deposits consist of a mixture of sand, silt, and clay, which contributes to the diverse types of soils of the city. The terrain is mostly flat in the central urban zones, with mild slopes that become sharper towards hills and the pre-Alpine region located to the west and north. The topographical heterogeneity plays a significant role in hydrological processes, such as surface runoff and flood risk, particularly in an urban development context. [3]. The choice to focus this thesis on District 6, located in the north-east part of Turin, is motivated by several factors. Firstly, this area combines various urban landscapes, including residential, industrial, and green spaces, making it a representative case study for hydrological analysis in an urban context. Moreover, District 6 includes critical watercourses, such as the Stura di Lanzo River and the Po River. Additionally, the availability of high-resolution data allows for an accurate spatial analysis within the framework of the SCS–CN model. Figure 2.1 shows the map of the study area, georeferenced to the UTM zone 32 N, WGS 84 projection, EPSG 32632. Since data requires a significant processing capacity, an area covering about 2 km^2 is selected. The chosen area is located at the confluence of the Po and Stura di Lanzo rivers, where land use is quite heterogeneous. This region offers a representative sample of the district, making it suitable for evaluating urban runoff dynamics under different land cover

conditions.

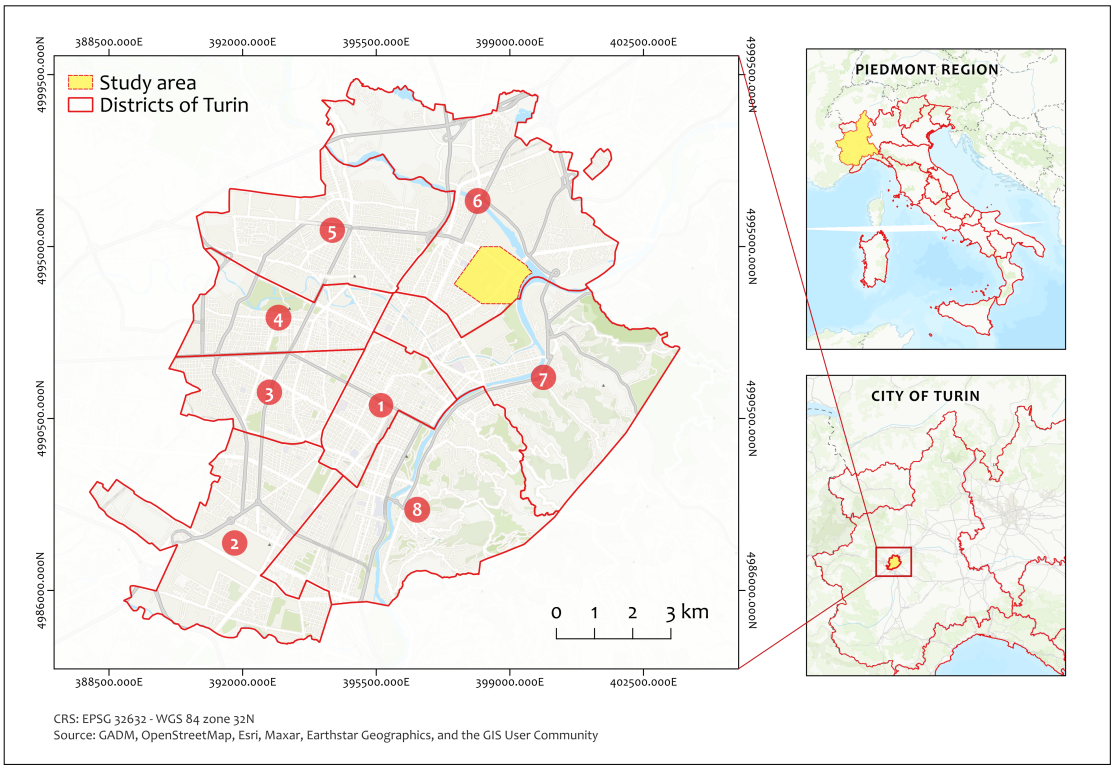

Figure 2.1: Location of the study area [4] [5]

2.2 Data Source and Methods

The point cloud was processed in ENVI LiDAR software to obtain a Digital Terrain Model (DTM), a Digital Surface Model (DSM), the building perimeter, and trees height and radius. These two features were used for a 3D representation of the study area using the ArcGIS Pro software. In a GIS environment, a validation of the DTM was performed. An ENVI supervised classification was needed to identify the remaining permeable and impermeable surfaces that were not included within the official cartography of the city. The ArcGIS Pro software allowed to reconstruct urban sub-catchments. During this process, a hybrid elevation model was used, as a combination of the bare-earth DTM with the building perimeter. The hydrological analysis was performed using the SCS-CN method to evaluate superficial runoff, given the land use within each sub-catchment, hydrological soil groups, and extreme rainfall data estimated for specific return periods and event durations.

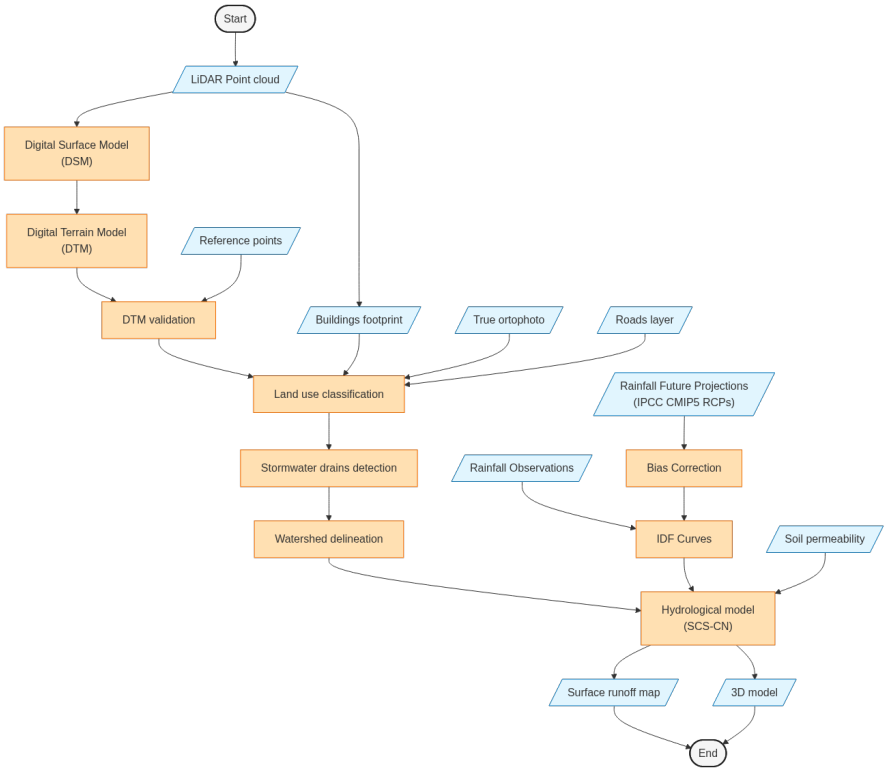

Figure 2.2: Workflow of the study

LiDAR Data

The dataset was acquired in 2022 by the company CGR, using the Leica CityMapper-2 hybrid oblique imaging and LiDAR sensor onboard an aircraft.

Table 2.1: Parameters of the LiDAR acquisition.

Parameter	**Value**	**Units**
Point density	30-40	pts/m^2
Measurement frequency	1600	Khz
Acquisition angle (FOV)	20	°
Flight height	1096	m

Data are referenced to UTM Zone 32N, WGS 84, and EPSG 32632. The true orthophoto of the study area has a resolution of 5 cm, while DTM and DSM processed in ENVI LiDAR have a resolution of 50 cm and 5 cm, respectively.

Land Use Data

Among the urban features available from the Municipal Technical Map (Carta Tecnica Comunale (CTC)) of Turin [6], the road network, tree layers, and official building footprints were utilized. Additionally, reference points from the same dataset were employed for the geometric validation of the DTM. Conversely, a second set of building vectors, hereafter referred to as LiDAR-derived building perimeters, was extracted directly from the point cloud through the automatic classification algorithm in ENVI LiDAR software. The distinction between these two building datasets was crucial for the methodology of this study, as detailed in Section 2.5, since they served different hydraulic and hydrological purposes. Feature classes not included in the previous ones were obtained from an ENVI supervised classification performed on the true orthophoto. The other key elements to take into consideration were stormwater inlets, which play a crucial role in determining watersheds and sub-catchments. These features were acquired using the SmartCITY3D [7] developed by Digitarca s.r.l.

Rainfall data

Rainfall observations were obtained from the Regional Environmental Protection Agency (Agenzia Regionale per la Protezione Ambientale ((ARPA)) Piedmont catalog [8], considering the "Serie Ultracentenarie" section for the period 1994-2024. Ultimately, rainfall future projections (2026-2070) were based on the COSMO-CLM regional climate model developed by Climate Limited-area Modelling (CLM Assembly) [9, 10, 11].

Table 2.2: Data category

Data Type	Description	Source/Provider	Period
LiDAR Point cloud	Raw altimetric data	CGR	2022
True ortophoto	5 cm resolution RGB aerial imagery	CGR	2022
Urban features	Road network, reference points, administrative boundary	CTC of Turin	2024
Urban features	Stormwater inlets	SmartCITY3D	2025
Rainfall observations	Historical time series	ARPA Piemonte	1994–2024
Climate projections	IPCC CMIP5 RCP 4.5 and RCP 8.5 scenarios	COSMO-CLM	1979–2005 2026–2070

2.3 LiDAR Data Processing

The outputs generated with ENVI LiDAR software are presented in this section. The DTM provides information on elevations of bare-earth terrain, which is essential to model flow paths, determine slope, and delineate watershed boundaries. The DSM includes surface features such as buildings and vegetation, essential for understanding how urban structures influence the flow and accumulation of rainwater. Together, DTM and DSM form the basis for an accurate estimate of surface runoff during intense rainfall events, helping to assess flood risk and urban drainage planning.

2.3.1 Digital Terrain Model

Figure 2.3 shows the DTM with a resolution of 50 cm. To better identify surface features in QGIS, the render type was set to "Singleband pseudocolor", then superimposed with a hillshade layer of the DTM.

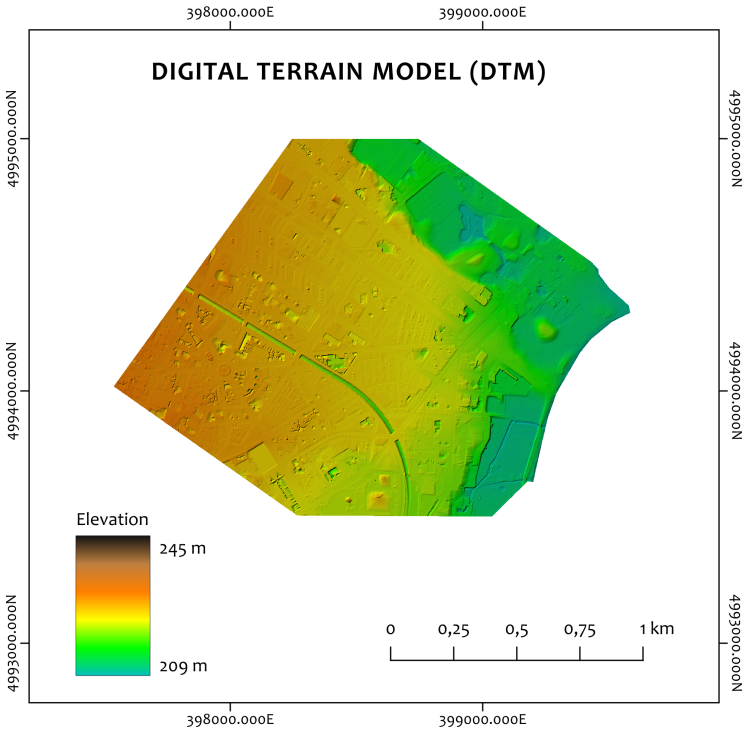

Figure 2.3: DTM

The elevation of the ground appears lower in areas covered by vegetation, whereas it is higher in zones with urban structures. This discrepancy may be attributed to the software's limited ability to fully remove surface objects during the generation of the DTM, leading to residual elevation artifacts.

DTM validation

To assess the accuracy of the DTM, a validation was carried out using reference elevation points extracted from the city of Turin geoportal catalog. According to the American Society of Photogrammetry and Remote Sensing (ASPRS) [12], the criterion that best represents elevation data quality is the vertical accuracy. The assessment requires independent ground-truth data, consisting of high-precision elevation measurements with the following characteristics:

- Not used in the DTM generation process
- Well distributed across the study area
- Higher accuracy with respect to the DTM
- At least 20 checkpoints in each of the major land cover categories are recommended for statistically significant results

The error relative to each checkpoint was calculated as the difference between the LiDAR measurement and the reference point interpolated at the same x/y coordinates. The following equations allowed to evaluate the elevation discrepancies for each point, the mean, the standard deviation, and the vertical root mean square error ($RMSE_z$).

$$Error_{(i)} = Z_{DTM,i} - Z_{REF,i} \tag{2.1}$$

$$\mu_{errors} = \frac{1}{n}\sum_{i=1}^{n} Error_{(i)} \tag{2.2}$$

$$\sigma_{errors} = \sqrt{\frac{1}{n-1}\sum_{i=1}^{n}(Error_{(i)} - \mu)^2} \tag{2.3}$$

$$RMSE_z = \sqrt{\frac{1}{n}\sum_{i=1}^{n} Error_{(i)}^2} \tag{2.4}$$

The initial set of reference points consists of 232 observations, of which 21 were excluded from the analysis, obtaining a set of 211 elements. The outlier exclusion threshold was set at $3 \times 1.4826 \times MAD$ (Median Absolute Deviation), according to the methodological approach discussed by Höhle and Höhle (2009) to handle

outliers and non-normal distributions [13]. Such outliers were excluded from the analysis, as large discrepancies could be caused by the presence of surface obstacles (e.g., vegetation, vehicles, or temporary structures). These elements can interfere with LiDAR measurements, compromising the reliability of the validation process.

Table 2.3: Statistical accuracy metrics of DTM elevation errors compared to reference points.

Parameter	**Value**
Minimum error	- 0.283 m
Maximum error	0.265 m
Standard deviation	0.088 m
Mean error	- 0.053 m
$RMSE_z$	0.103 m
95^{th} percentile	0.098 m

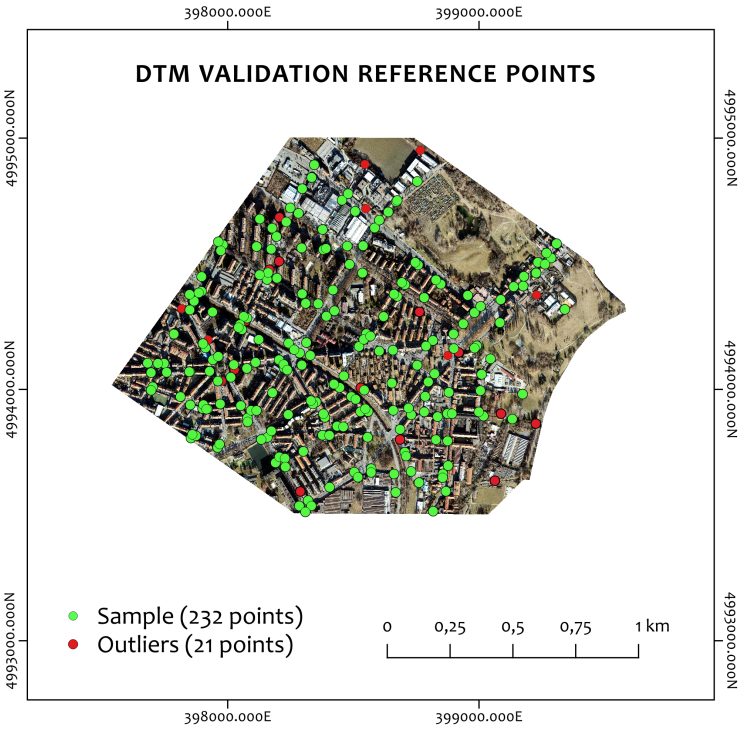

Figure 2.4: Reference points and outliers for DTM validation

According to ASPRS standards [12], vertical accuracy for complex land cover

types, the 95th percentile method shall be used, as errors in these areas do not typically follow a normal distribution. The 95th percentile of 0.098 m on a DTM grid size of 0.5 m demonstrates that the error distribution is tightly clustered around the zero-mean. This level of precision ensures that the DTM acts as a highly reliable surface for urban runoff simulations.

2.3.2 Digital Surface Model

Figure 2.5 displays the Digital Surface Model (DSM) with a resolution of 0.05 m. High-resolution DSMs are essential for urban flood modeling, for capturing small-scale surface elements, such as buildings, curbs, walls, and vegetation that influence overland flow patterns.

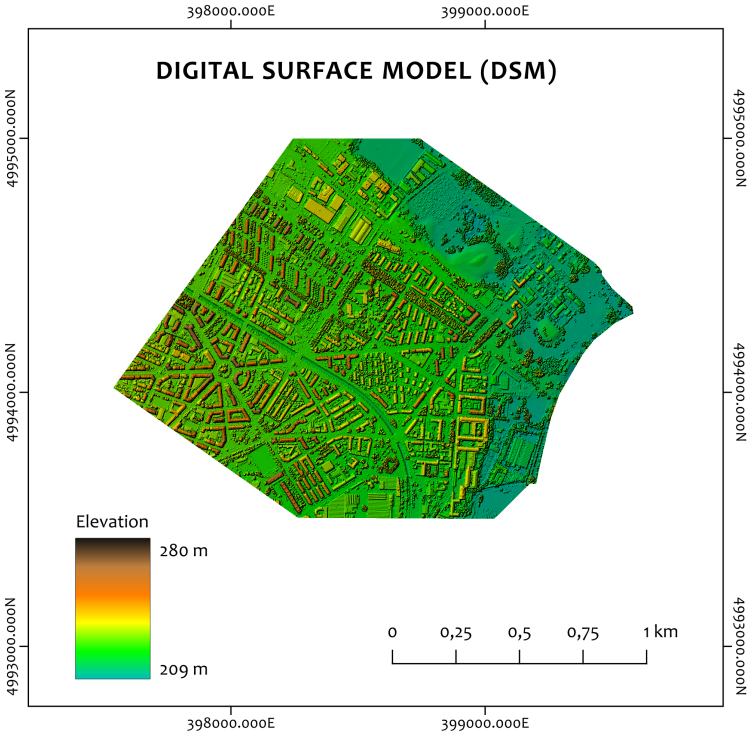

Figure 2.5: DSM

DSM validation

The validation of DSM was carried out considering the 232 reference points used for the DTM validation. A further outlier exclusion was performed using the robust MAD filter, resulting in a final validation dataset of 132 points.

Table 2.4: Statistical accuracy metrics of DSM elevation errors compared to reference values.

Parameter	Value
Minimum error	- 0.534 m
Maximum error	0.724 m
Standard deviation	0.136 m
Mean error	- 0.068 m
$RMSE_z$	0.152 m
95^{th} percentile	0.141 m

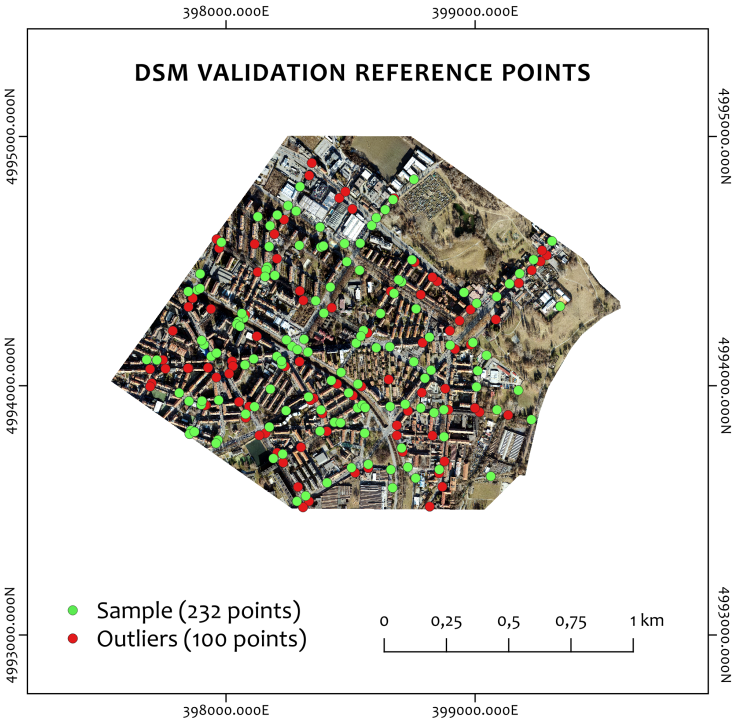

Figure 2.6: Reference points and outliers for DSM validation

The DSM validation resulted in an RMSEz of 0.152 m and a 95th percentile of

0.141 m. This result proves that the measurement stability of the LiDAR sensor remains highly reliable, although discrepancies between the DSM and the reference cartography are expected in an urban environment due to temporal differences and geometric complexities.

2.4 Features Extraction

In the following section, the methodology adopted to extract key urban features that require additional spatial refinement is reported.

2.4.1 Road Extraction

The road network includes both vehicles and pedestrian circulation pathways. Although the two vector layers do not correctly overlap with the true orthophoto. A further refinement was performed using QGIS software using the georeference tool. More in detail, 14 ground control points were selected on the true orthophoto, corresponding to visible sharp corners of sidewalks or buildings. In figure 2.7, the points selected are shown, with their coordinates and horizontal and vertical shift with respect to the road network layer.

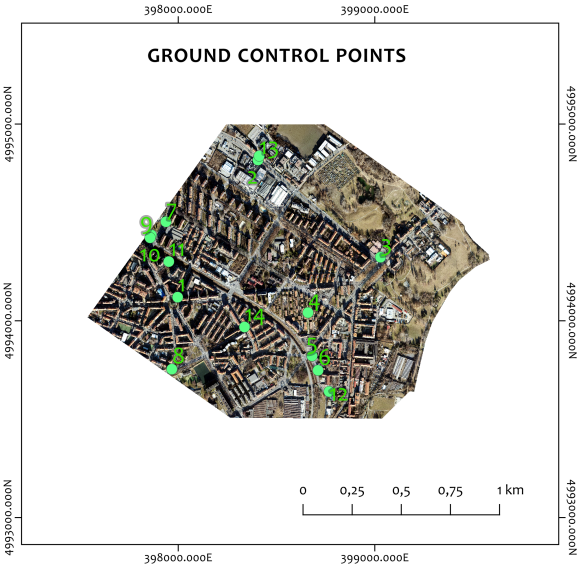

ID	X	Y	dX	dY	Residual
1	397996,46	4994119,66	-3,10	5,59	6,39
2	398405,40	4994817,10	1,09	-0,11	1,10
3	399028,98	4994322,72	-0,26	0,33	0,42
4	398660,09	4994041,09	-6,58	1,89	6,85
5	398680,73	4993821,34	8,12	0,5	8,13
6	398711,29	4993747,77	-3,62	-1,40	3,88
7	397937,14	4994503,15	0,24	-5,43	5,44
8	397967,10	4993753,70	4,10	-1,38	4,33
9	397862,35	4994435,52	0,41	2,35	2,38
10	397856,34	4994421,73	6,71	-3,85	7,74
11	397951,49	4994300,62	-1,41	7,50	7,63
12	398767,57	4993639,84	0,85	-2,54	2,68
13	398411,68	4994837,57	1,48	-0,8	1,68
14	398337,03	4993968,10	-1,93	2,32	3,02

Figure 2.7: Ground control points for road network georeference

2.4.2 Stormwater inlets extraction

Stormwater inlets were identified using SmartCity3D software, placing georeferenced markers while navigating through street-level images. It is important to note that, in some cases, street-level images were taken only from one side of the roadway or in locations where inlets were not easily accessible. After the acquisition phase, a refinement was performed using Google Earth Pro software to identify the remaining undetected assets. Figure 2.8 shows 1922 elements detected considering both methods.

In order to standardize the hydrological analysis, it was chosen to map only the square grid storm inlets (typical dimensions 50x50 cm). This choice is justified by the fact that this typology constitutes the predominant construction standard for ordinary roads in the Municipality of Turin, covering almost all primary road drainage assets. Furthermore, linear grids (typically found in private ramps or pedestrian plazas) were excluded. Their collection capacity would require detailed field surveys, which fall beyond the objectives of this analysis.

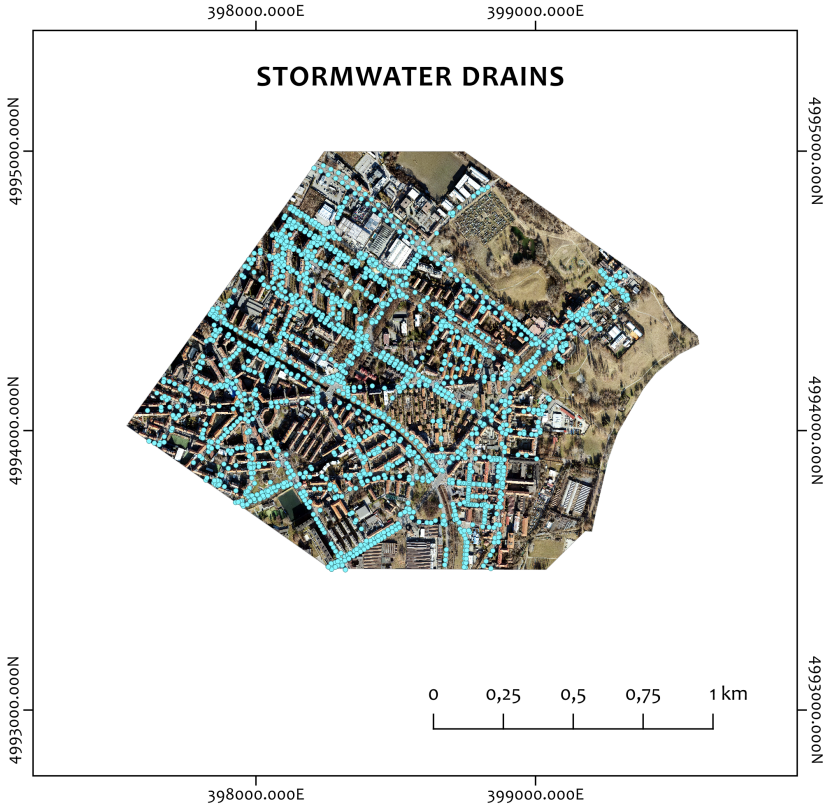

Figure 2.8: Detected stormwater inlets

2.4.3 ENVI land use classification

Among the classification methods tested on ENVI software, Maximum Likelihood Classification (MLC) reached the highest overall accuracy. Prior to classification, road networks, building footprints, water bodies, and shadows were removed from the true orthophoto using inverse masking to isolate and classify only the remaining surface. More specifically, the shadow feature was extracted from a color slice related to band 1 of the stretched true orthophoto. The range of digital numbers (DN) associated with shadows was selected from 0 to 120.

The classification focused on the following land cover classes:

- Impermeable surfaces (parking lots, roofs, driveways)
- Sparse vegetation
- Trees

The first step of the workflow involved the application of a root-squared stretch to enhance the radiometric contrast of the true orthophoto, followed by the application of the MLC algorithm. As a result, the confusion matrix (Table 2.5) indicated an overall classification accuracy of 90.89%.

Table 2.5: Confusion matrix using ground-truth ROIs

Class	Sparse vegetation (TRUTH)	Trees (TRUTH)	Impermeable surfaces (TRUTH)	Total (%)
Sparse vegetation	99.90	2.69	0.88	71.63
Trees	8.85	89.22	2.14	22.29
Impermeable surfaces	0.26	8.09	96.99	6.08
Unclassified	0.00	0.00	0.00	0.00
Total (%)	100.00	100.00	100.00	100.00

Figure 2.9 shows the mean DN values in the three spectral bands for each land cover class, based on both training ROIs and ground truth samples. The curves of ground truth ROIs are mostly aligned with the training data, confirming the consistency of the samples used for the supervised classification. However, remarkable discrepancies are observed within the tree class, where the ground truth profile differs more significantly from the training ROI. This divergence may be attributed to intra-class variability due to different tree species, canopy density, or shadow effects, which can influence the classification accuracy. In contrast, impermeable surfaces and sparse vegetation maintain a more stable spectral behavior across training and validation samples.

Figure 2.10 shows the final classification combined with masked layers (building footprints, road network, water bodies). In particular, the road network is included within the "Impermeable surfaces" class.

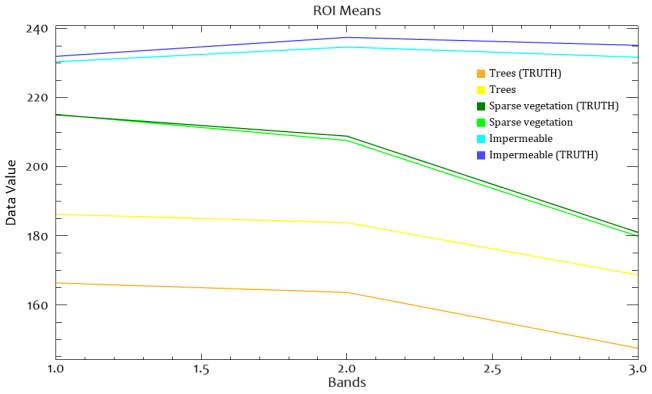

Figure 2.9: ROIs mean values

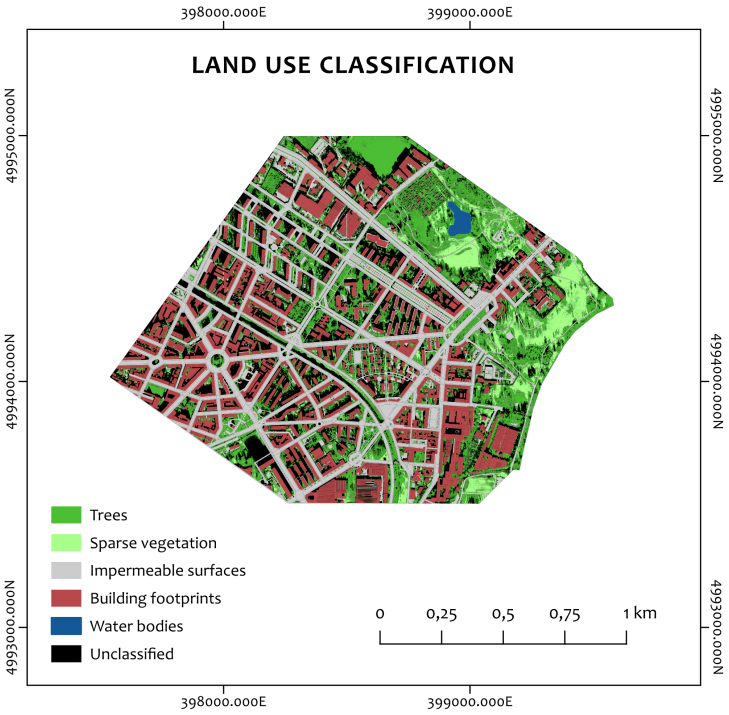

Figure 2.10: ENVI land use classification

2.5 Watershed Delineation

The study area was divided into sub-basins through the delineation of watershed lines. The latter represent imaginary boundaries from which water flows in different directions, contributing to neighboring watersheds. The process used was implemented in ArcGIS Pro, considering as input a raster consisting of the DTM and the building height derived from the DSM. For this purpose, a binary mask was created from the building perimeters vector obtained by processing the point cloud on ENVI LiDAR. Contrary to the ENVI classification of the true orthophoto (Sub-Section 2.4.3), the official building footprint vector derived from the Municipal Technical Map was not used, since the latter is made up of small elements that could interfere with the flow of water. The choice of using LiDAR-derived building perimeters was necessary to ensure spatial consistency between the DSM and obstacles. Using such an input model, permanent objects that would have been considered obstacles to the stormwater path were excluded.

The ArcGIS Pro tools used in the process were as follows:

1. Fill sink tool to remove imperfections in the data. The z-limit was set at 2 m, defining the maximum difference allowed between the depth of a sink and the pour point;
2. Flow direction tool using the flow modeling algorithm D8. The latter models flow direction from each cell to its steepest downslope neighbor;
3. Flow accumulation tool using the flow modeling algorithm D8. The result is a raster of accumulated flow to each cell, as determined by accumulating the weight for all cells that flow into each downslope cell;
4. Snap Pour Point tool to search within a snap distance set to 5 m around the specified pour points (detected storm drains) for the cell of highest accumulated flow and move the pour point to that location;
5. Watershed tool to determine the contributing area above a set of cells;
6. Conversion of the watershed raster to polygon (Figure 2.11);
7. Zonal Statistics as Table tool to summarize the values of the raster representing Curve Number (CN) values (detailed in Sub-Sub-Section 2.7.5, Table 2.10), within watershed polygons, and reports the results as a table. The statistics calculation type selected was the mean.
8. Join the table to the watershed layer.

It is important to note that areas of private property (courtyards, residential complexes) were not covered by the survey of the drainage network, and no artificial drain nodes were assigned to such sub-basins. As a result, these areas will appear as high flood risk due to the lack of stormwater inlets. This representation does not necessarily indicate physical flooding, suggesting the need to integrate data from private networks in the future.

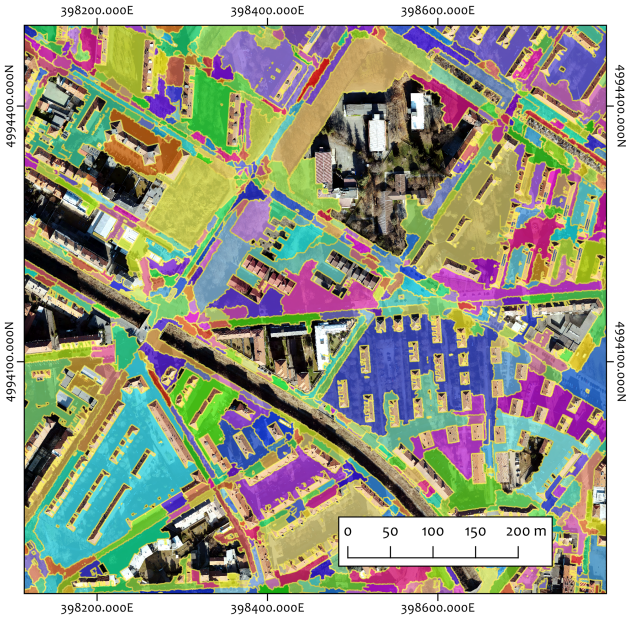

Figure 2.11: Watersheds delineation result

2.6 Drainage Network Conveyance Capacity

The maximum conveyance capacity of the inlets was not derived from the capacity of the road grid, but rather from the conveyance capacity of the pipe connecting the sump to the sewer system. This methodological choice was cautionary, since the lowest capacity of the two capacities was considered the limiting factor of the system. It was therefore assumed that the accumulation of water on the surface coincides with the achievement of uniform flow at the full cross-section of the connection duct. The pipeline design was derived from the Integrated Water Service regulations published by Società Metropolitana Acque Torino (SMAT) [14]. According to Art. 29, unpolluted waters include stormwater from impermeable surfaces, roofs, terraces, and urban roads. The channel size is regulated in Art. 32, according to which the minimum internal diameter (D) must be equal to 160

mm with a minimum slope (i) equal to 1.5% for rainwater. The calculation of the maximum conveying flow rate was performed by applying Chezy's Formula (Eq. 2.5) using the Gauckler-Strickler roughness coefficient(K_s) [15]. The latter was uniformly assigned throughout the study area, in the absence of geometric and hydraulic data. Therefore, a value of $K_s = 80\ m^{1/3}/s$ was chosen for concrete pipes with slight encrustations, thus adopting a precautionary approach.

$$Q_{\max} = A \cdot K_s \cdot R^{2/3} \cdot \sqrt{i} \tag{2.5}$$

Where

- $Q_{\max}$ is the maximum conveyance capacity (m^3/s);
- A is the cross-sectional area of the tube (m^2) as $\pi \cdot D^2/4$;
- K_s is the Gauckler-Strickler roughness coefficient ($m^{1/3}/s$);
- R is the hydraulic radius (m) for a full circular cross-section as $D/4$;
- i is the longitudinal slope of the pipeline (m/m).

The resulting $Q_{max} = 23.04\ \frac{L}{s}$ was compared with the estimated surface runoff of each sub-basin (calculations detailed in Sub-Sub-Section 2.7.5). In Section 3, flood vulnerability maps visualize the criticality of the drainage network.

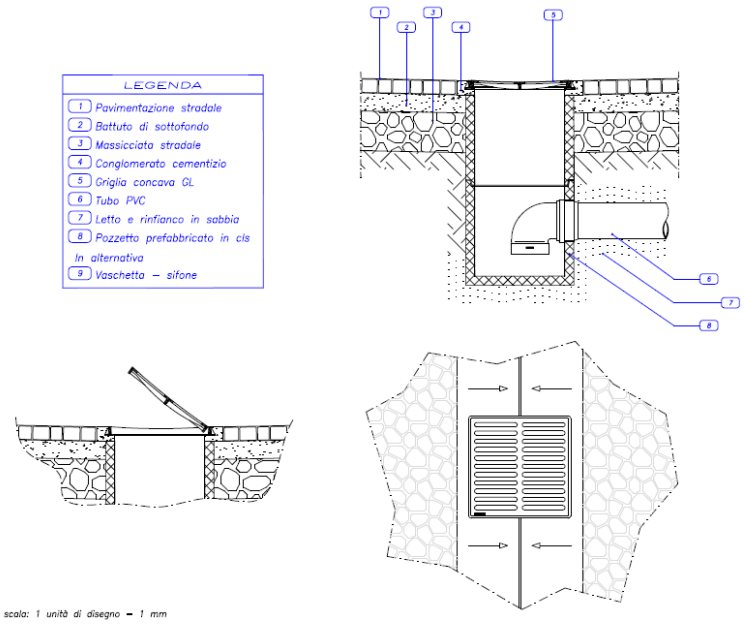

Figure 2.12: Example of a concave grid inlet [15]

2.7 Hydrological Analysis

2.7.1 Extreme value distribution

Since the main objective of this study was to estimate surface runoff under extreme weather events, the Annual Maxima Series (AMS) was derived using ARPA Piemonte observations to simulate critical hydrological scenarios. The AMS from 1994 to 2024 was used to calculate the non-exceedance frequency $F(x)$ of the sample as in Eq. 2.6, where k is the ranking and n the sample elements. [16]

$$F(x) = \frac{k}{n+1} \tag{2.6}$$

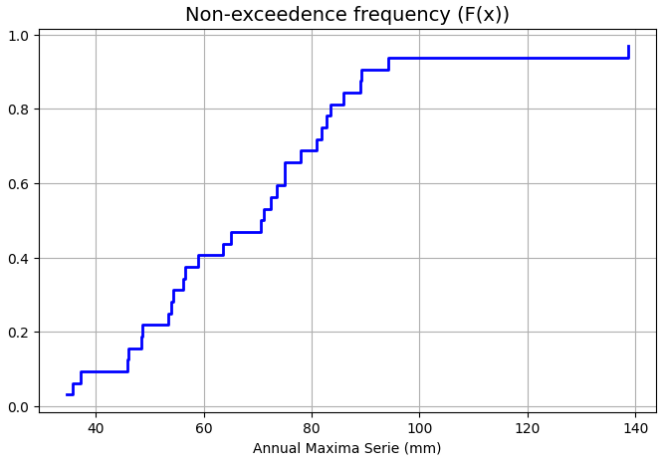

Figure 2.13: Non-exceedance frequency of the rainfall observations AMS

The AMS was modeled using the Extreme Value Type I (EVI) probability distribution (Eq. 2.7), which is the most commonly applied model for storm rainfall analysis [16].

$$F(x)_{EVI} = exp\left[-exp\left(-\frac{x-u}{\alpha}\right)\right] \tag{2.7}$$

Where

- $\alpha = \frac{\sqrt{6}s}{\pi}$
- $u = \bar{x} - 0.5772\alpha$

It is worth noting that one value stands out as a potential outlier, corresponding to the flood event of 1994. However, since the EVI distribution is specifically suitable for modeling extreme events, this value was retained in the analysis.

A reduced variate can be defined as

$$y = \frac{x_{EVI} - u}{\alpha} = -ln\left[ln\left(\frac{1}{F(x)}\right)\right] \tag{2.8}$$

Figure 2.14 shows in blue the probability plot that compares the observed values (x) with the reduced variate (y), the latter calculated as a function of the empirical frequency $F(x)$ derived from Eq. 2.6. The dashed red line represents the rainfall depths estimated using the EVI distribution (x_{EVI}), according to Eq. 2.8. The Pearson correlation coefficient between x and y was calculated to be 0.968, indicating a strong linear correlation. Table 2.6 shows the mean and standard deviation for the observed and estimated values.

Table 2.6: Mean and standard deviation of observed and estimated rainfall depth

Statistic	Observed	EVI
Mean (mm)	67.76	67.09
Standard deviation (mm)	21.43	18.96

In Figure 2.15, the estimated rainfall depth ($x_{EVI,T}$) was derived from the reduced variate (y_T) calculated as a function of the return period T, according to Eq. 2.9, where T indicates periods shorter than 50 years. Also, observed values were derived as a function of T (x_T), calculating the empirical frequency ($F(x)_T$) as shown in Eq. 2.10.

$$y_T = -ln\left[ln\left(\frac{T}{T-1}\right)\right] = \frac{x_T - u}{\alpha} \tag{2.9}$$

$$F(x)_T = 1 - \frac{1}{T} \tag{2.10}$$

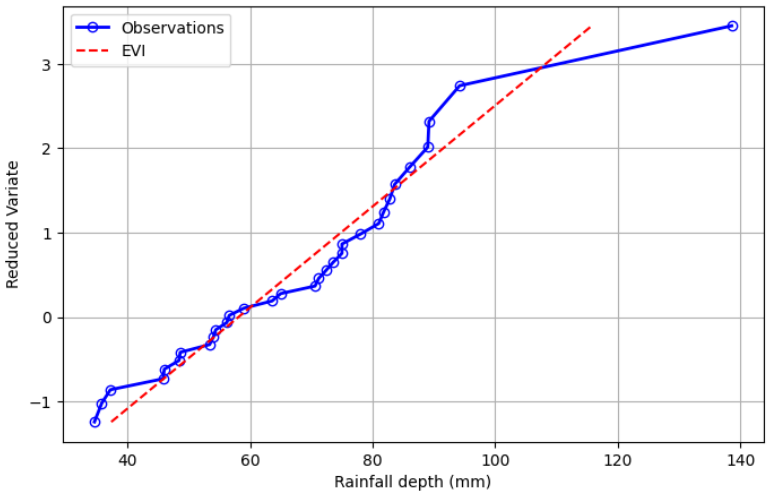

Figure 2.14: Probability plot for EVI distribution

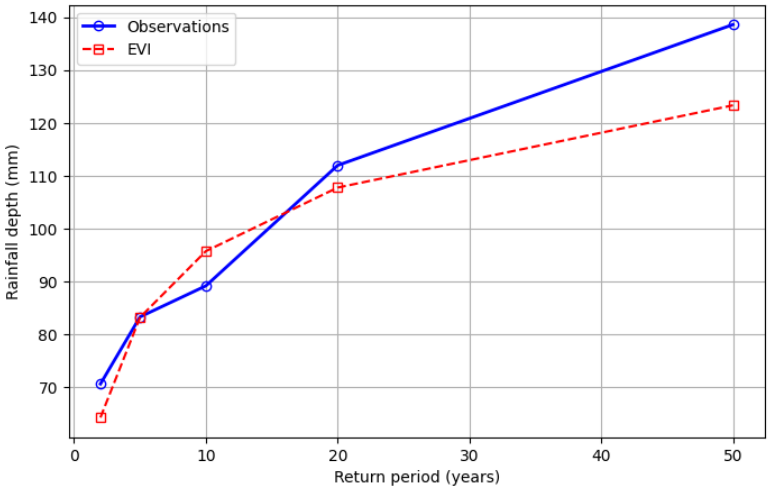

Figure 2.15: Return period against rainfall depth

2.7.2 Goodness-of-Fit Assessment

Anderson Darling Test

Statistical validation of the probabilistic model was performed using the Anderson-Darling test. This test evaluated the null hypothesis (H_0) that a sample was extracted from a population that follows a particular distribution. The analysis was performed using the Python programming language with the *scipy.stats.anderson* function [17], specifying the *"gumbel_r"* type of distribution (Gumbel Right-skewed). This configuration ensures that the model correctly addresses the distribution of

maxima, where the distribution tail extends towards positive infinity. The following results were obtained:

- Calculated statistic (A^2): 0.4362
- Critical value ($\alpha = 0.05$): 0.731

The calculated test statistic is lower than the critical value at the 5% significance level. Therefore, there is insufficient statistical evidence to reject the null hypothesis. The analysis confirms that the EVI distribution provides a statistically valid fit for the dataset.

Mean Average Error (MAE) and Root Mean Squared Error (RMSE)

The MAE was calculated as the mean of the absolute residuals between estimated data x_{EVI} and the original values x (Eq. 2.11). The resulting MAE is equal to 3.74 mm.

$$MAE = \frac{1}{n}\sum_{i=1}^{n}|x_{EVIi} - x_i| \tag{2.11}$$

The RMSE was calculated as the square root of the mean squared errors (Eq. 2.12). This indicator is more sensitive to outliers, penalizing large errors more than MAE. The resulting RMSE is equal to 5.60 mm.

$$RMSE = \sqrt{\frac{1}{n}\sum_{i=1}^{n}(x_{EVIi} - x_i)^2} \tag{2.12}$$

Being higher than the MAE, RMSE reflects the model's sensitivity to larger residuals. RMSE and MAE values indicate a perfect fit if close to zero. However, values less than half of the standard deviation of the observations may be considered low [18]. The standard deviation of the observed data was 21.43 mm (Table 2.6, Sub-Sub-Section 2.7.1). Consequently, the calculated RMSE and MAE were well below the threshold ($\approx$ 10.7 mm), confirming the high accuracy of the EVI probability distribution.

Nash-Sutcliffe Efficiency (NSE)

The Nash-Sutcliffe Efficiency (NSE) is defined as the measure of the relative magnitude of the residual variance compared to the observations' variance (Eq. 2.13). The index ranges between -∞ and 1.0, where the latter is considered the optimal value. Generally, values between 0.0 and 1.0 are considered acceptable [18].

$$NSE = 1 - \frac{\sum_{i=1}^{n}(Y_i^{obs} - Y_i^{EVI})^2}{\sum_{i=1}^{n}(Y_i^{obs} - Y^{mean})^2} \tag{2.13}$$

Where

- Y_i^{obs} is the ith observation,
- Y_i^{EVI} is the ith estimated value using EVI probability distribution,
- Y^{mean} is the mean of the observations.

The NSE was calculated to be 0.9294, representing a satisfactory result.

2.7.3 Intensity-Duration-Frequency (IDF) Curves

The determination of the Intensity-Duration-Frequency (IDF) curves was based on the statistical analysis of ARPA Piemonte observations covering the 31 years from 1994 to 2024. IDF curves describe the link between the value of the average intensity and the duration of a precipitation event, which is associated with a return time T. The latter is defined as the average number of years that is needed to wait for the corresponding intensity value to be exceeded. Intensity represents the time rate of precipitation (mm/h). The common expression used to calculate the mean intensity is shown in Eq. 2.14 [16].

$$i = \frac{P}{d} \tag{2.14}$$

where

- P is the rainfall depth (mm)
- d is the event duration (h)

The analytical formulation most widely used in Italy for IDF curves for durations of 1-24 hours is shown in Eq. 2.15 [19].

$$i(d) = a \times d^{n-1} \tag{2.15}$$

where

- a is the hourly rain coefficient
- n is the scale variance exponent

According to the Atlas of Intense Rainfall in Piedmont published by ARPA Piemonte [20], the coefficients a and n for the municipality of Turin are 29.21 and 0.26, respectively. Due to the unavailability of sub-daily records for the entire timeframe, a temporal disaggregation was applied to the daily rainfall depths. The equation used for this purpose was obtained starting from Eq. 2.15, calculating the rainfall depth P as in Eq. 2.14.

$$P = i \times d = a \times d^{n-1} \times d = a \times d^{n} \tag{2.16}$$

Later, an expression was derived to estimate the rainfall depth for any sub-daily duration from 1 to 24 hours (P_d), given the rainfall depth on a daily basis (P_{24}).

$$\begin{aligned} P_d &= a \times d^n \\ P_{24} &= a \times 24^n \\ P_d &= P_{24} \times \left(\frac{d}{24}\right)^n \end{aligned} \tag{2.17}$$

Data processing was performed in a Python environment. The AMS was extracted from daily records and consequently disaggregated according to Eq. 2.17 for event durations of 1 hour, 3 hours, and 6 hours (Figure 2.16).

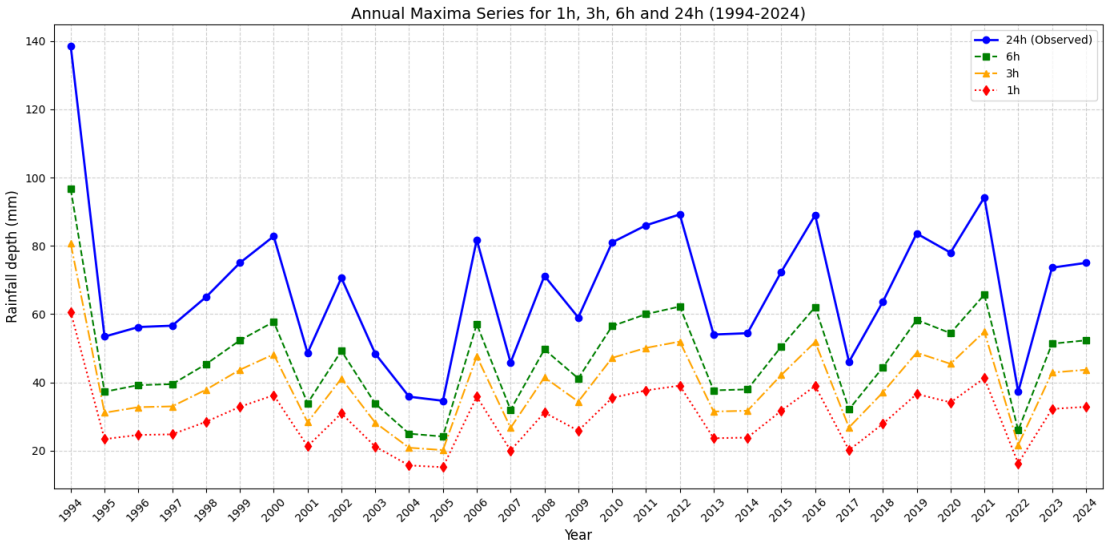

Figure 2.16: Rainfall depth for 1h, 3h, 6h, and 24h.

Assuming that the EVI distribution is applicable, as analyzed in the Sub-Sub-Section 2.7.2, the rainfall depth for a given T is determined by Eq. 2.18 [16].

$$x_{T,T_d} = \bar{x_{T_d}} + K_T \times s_{T_d} \tag{2.18}$$

Where

- $\bar{x_{T_d}}$ is the mean of rainfall depths for a specific duration T_d
- s_{T_d} is the standard deviation of rainfall depths for a specific duration T_d
- K_T is the frequency factor (Eq. 2.19)

$$K_T = -\frac{\sqrt{6}}{\pi}\left[0.5772 + ln\left(ln\frac{T}{T-1}\right)\right] \tag{2.19}$$

In Figure 2.17, IDF curves were reported. The values of rainfall intensity were also reported in Table 2.7, resulting consistent with the Atlas of Intense Rainfall in Piedmont by ARPA Piemonte.

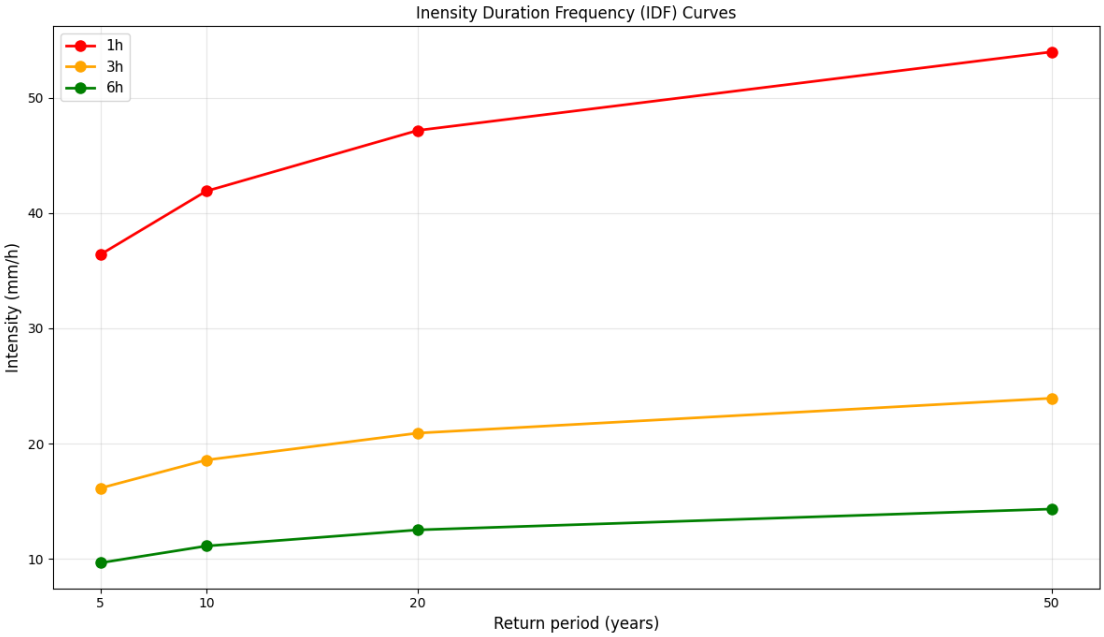

Figure 2.17: Intensity-Duration-Frequency (IDF) Curves

Table 2.7: Rainfall intensity (mm/h) for event duration and return period

	1 Hour	3 Hours	6 Hours
T = 5	36.41	16.15	9.67
T = 10	41.89	18.58	11.12
T = 20	47.16	20.92	12.53
T = 50	53.97	23.94	14.33

2.7.4 Future Projections

To simulate urban surface runoff in future scenarios, a high-resolution (about 8 km) climate simulation over Italy was considered. The dataset is the result of a dynamic downscaling process developed by Climate Limited area Modelling Assembly (CLM Assembly), produced with COSMO-CLM [9]. Data are available over the period 2006-2070 for the IPCC CMIP5 scenarios RCP4.5 and RCP8.5, and over the control period 1979-2005 [10, 11]. Regional Climate Models (RCMs) should be handled with caution, as they can present significant biases due to systematic model errors. Some typical biases include underestimating or overestimating seasonal variations in precipitation, or having too many wet days with low-intensity rain. Therefore, the application of a bias correction is recommended [21]. In the following paragraphs, the bias correction process and the calculation of IDF Curves were reported, considering the projection period 2026-2070.

Bias Correction

Bias correction methods aim to transform climate simulations in such a way that the statistical properties are comparable with those of the reference series. The process used in this study for bias correction is the "quantile-mapping" (QM) method, where daily rainfall data from ARPA Piemonte, also considered for the hydrological analysis in the Sub-Section 2.7, were considered as reference series along the period common to the COSMO-CLM climate model (1979-2005). The process was implemented in a Python environment and included two phases:

1. Training phase (calibration): Given the variable x_{mod} (daily precipitation) from the COSMO-CLM model, the QM method corrects it by defining a transfer function based on the common historical period (Eq. 2.20)[22].

$$P_{corr} = F_{oss}^{-1}\left(F_{mod}(X_{mod})\right) \tag{2.20}$$

Where

- F_{mod} is the CDF of the variable x_{mod}
- F_{oss} is the inverse CDF of ARPA Piemonte observations

2. Correction phase: The transfer function is applied to future data (IPCC CMIP5 RCP 4.5 and RCP 8.5 scenarios)

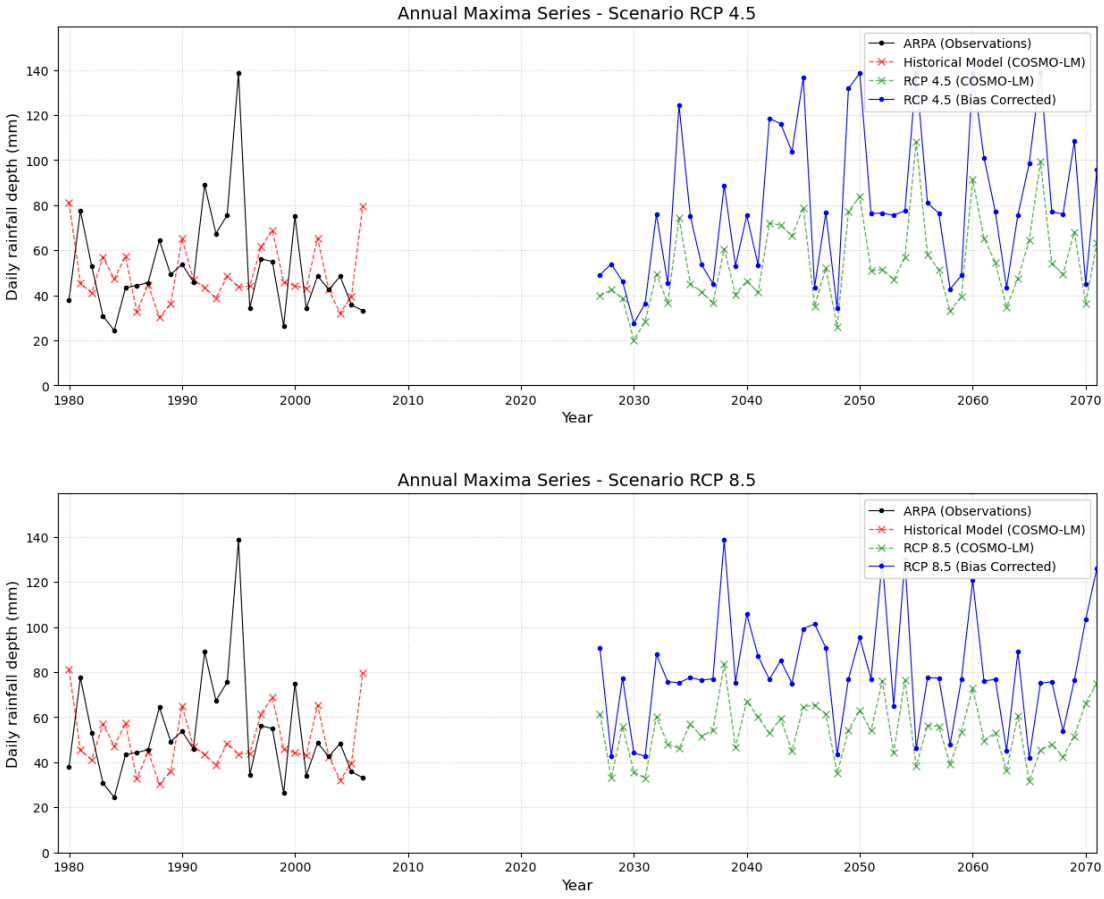

Figure 2.18: Unbiased AMS for RCP 4.5 and RCP 8.5 from COSMO-CLM model

IDF Curves

The IDF curves were obtained according to the procedure presented in the Sub-Sub-Section 2.7.3, considering the daily rainfall AMS corrected by bias over the period 2026-2070.

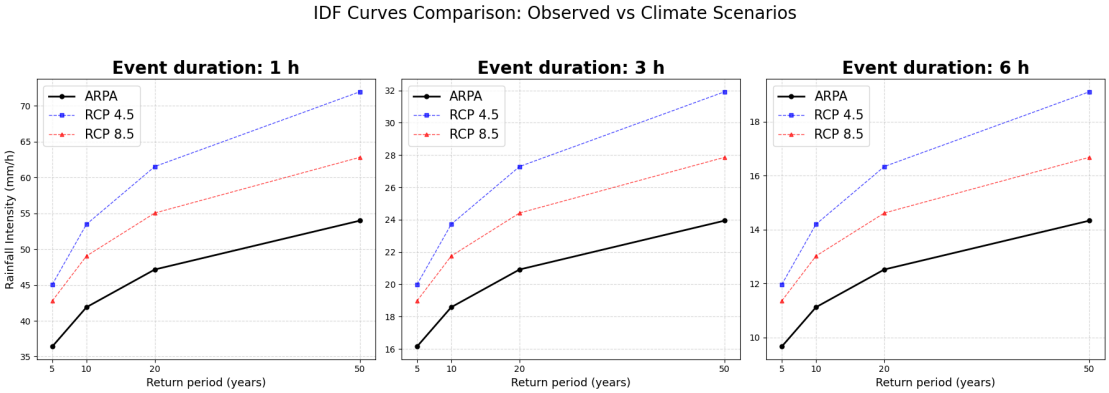

Figure 2.19: IDF curves for observations and future projections

Table 2.8: Comparison of rainfall intensities (mm/h) between the ARPA baseline (1994-2024) and COSMO-CLM RCPs future scenarios (2026-2070)

Event duration	**T**	**ARPA**	**RCP 4.5**		**RCP 8.5**	
(h)	(years)	(mm/h)	(mm/h)	$\Delta\%$	(mm/h)	$\Delta\%$
1	5	36.41	45.07	+23.8	42.78	+17.5
	10	41.89	53.47	+27.6	49.04	+17.1
	20	47.16	61.53	+30.5	55.05	+16.7
	50	53.97	71.96	+33.3	62.82	+16.4
3	5	16.15	19.99	+23.8	18.97	+17.5
	10	18.58	23.72	+27.7	21.75	+17.1
	20	20.92	27.29	+30.4	24.41	+16.7
	50	23.94	31.92	+33.3	27.86	+16.4
6	5	9.67	11.97	+23.8	11.36	+17.5
	10	11.13	14.20	+27.6	13.02	+17.0
	20	12.52	16.34	+30.5	14.62	+16.8
	50	14.33	19.11	+33.4	16.68	+16.4

2.7.5 SCS-CN Hydrological Model

The Soil Conservation Service (SCS, 1972) developed the Curve Number (CN) method to estimate the excess rainfall (or direct runoff) from a storm. SCS-CN hypothesizes that the ratio of the actual retained water and direct runoff to the respective potential quantities follows Eq. 2.21, and the continuity principle of Eq. 2.22 [16].

$$\frac{F_a}{S} = \frac{P_e}{P - I_a} \tag{2.21}$$

$$P = P_e + I_a + F_a \tag{2.22}$$

Where

- F_a is the actual water retained (in)
- S is the potential maximum retention (in)
- P_e is the direct runoff (in)
- P is the depth of precipitation (in)
- I_a is the initial abstraction before ponding (in)

Combining Eq. 2.21 and 2.22, the resulting P_e is expressed in Eq. 2.23.

$$P_e = \frac{(P - I_a)^2}{P - I_a + S} \tag{2.23}$$

From several studies conducted for small watersheds, the empirical relationship defining I_a is shown in Eq. 2.24.

$$I_a = 0.2S \tag{2.24}$$

The plots representing P_e as a function of P allowed to obtain curves later standardized with the introduction of the CN, related to S as shown in Eq. 2.25.

$$S = \frac{1000}{CN} - 10 \tag{2.25}$$

The SCS-CN model selects CN values based on several factors, including land use, hydrological soil group (HSG) type, and antecedent moisture condition (AMC) for runoff estimation. In this study, the average antecedent moisture condition (AMC II) was considered, which is the main one used for design applications [23].

According to SCS soil scientists, soils are classified into four HSGs based on the rate of infiltration and water transmission. Table 2.9 shows the ranges of values for HSGs classification.

Table 2.9: Hydrological Soil Groups according to water transmission rate

HSG	**Soil Texture**	**Water transmission rate** (in/hr)
A	Sand, loamy sand, or sandy loam	>0.30
B	Silt loam or loam	0.15 - 0.30
C	Sandy clay loam	0.05 - 0.15
D	Clay loam, silty clay loam, sandy clay, silty clay, or clay	0 - 0.05

The hydrogeological cartography from the Piedmont geoportal catalog [24] was considered to identify the equivalent vertical hydraulic conductivity of the unsaturated zone (Fig. 2.20). The latter was calculated by considering the thickness of the unsaturated zone divided by the sum of the ratios between the thickness of each lithological level and its own hydraulic conductivity.

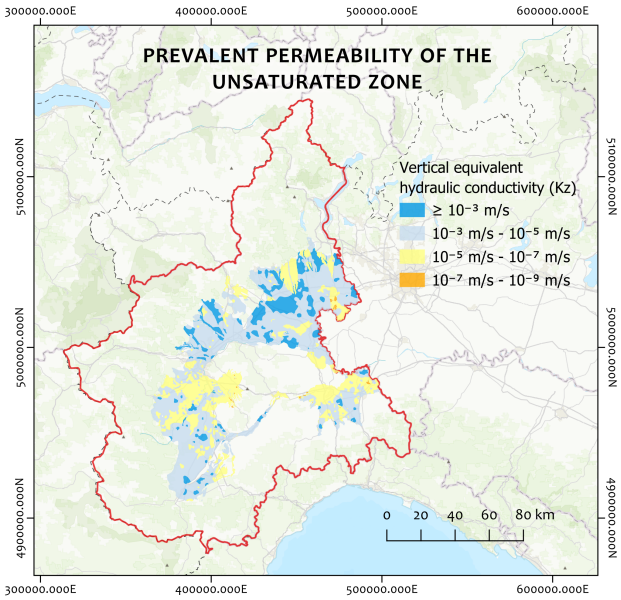

Figure 2.20: Equivalent permeability of the unsaturated zone

Within the study area, two prevalent condictivity classes were found, which were compared to the standard values from Table 2.9 to extract the corresponding HSGs. Overall, the HSG "A" was considered for subsequent runoff estimation. Tab. 2.10 shows the CN values used for land use, hydrological conditions, and HSGs according to USDA TR-55 [23]. A CN value was assigned to each pixel of a raster according to the land use classification (Sub-Sub-Section 2.4.3); consequently, a weighted average CN was calculated for each sub-basin (Section 2.5).

Table 2.10: Curve Numbers for land cover type, hydrological conditions, and hydrological soil group

Cover type and hydrological condition	**HSG Type**			
	A	B	C	D
Paved parking lots, roofs, driveways, etc. (exluding right-of-way)	98	98	98	98
Open space (lawns, parks, golf courses, cemeteries, etc.) in good conditions (grass cover >75%)	39	61	74	80
Woods—grass combination (orchard or tree farm) in good conditions	32	58	72	79

The implementation of Eq. 2.23 took place in a GIS environment for each sub-basin, considering the following inputs:

- Rainfall scenarios (Table 2.7) during the reference period 1994-2024,
- Future RCP 4.5 scenarios (Table 2.8) over the period 2026-2070,
- A raster of CN values (Table 2.10) based on the land use classification (Sub-Section 2.4.3).

Chapter 3

Results

This section presents the outcomes of the spatial hydrological modeling adopted in the study. First, a total of 12 vulnerability maps were produced to assess the criticality of the drainage system. The ratio between the generated runoff (according to the SCS-CN method) and the estimated maximum conveyance capacity of each sub-basin was calculated. Consequently, four vulnerability classes were defined as shown in Table 3.1. In particular, a ratio greater than 1 indicates a drainage system overload. The scenarios were developed starting from ARPA Piemonte observations over the period 1994-2024, considering return periods of 5, 10, 20, and 50 years, and event durations of 1, 3, and 6 hours. The same approach was applied to future projections, considering the bias-corrected RCP 4.5 scenario (from the COSMO-CLM climate model). To assess hydraulic vulnerability, a reduction coefficient of drainage network efficiency of 50% was introduced. This choice simulated realistic operating conditions, sometimes associated with partial obstruction of the collection grids caused by lack of maintenance or sudden debris supply. This section only reports flood vulnerability maps of the worst-case scenario for both datasets, considering the 1-hour event duration and 50% clogging coefficient. The complete atlas of the flood vulnerability maps and tables can be consulted in Appendix A. Later, a 3D model of the study area was developed, with the aim of visualizing buildings, trees, and the accumulated water level. In particular, the buildings were extruded from the DSM and the perimeters previously extracted from the point cloud. Trees were represented based on extrapolated attributes from the Municipal Technical Map of Turin. In particular, the average height was considered for each species, the latter grouped into six macro-classes (columnar, large conifer, umbrella conifer, standard broadleaf, ornamental, weeping). Ultimately, a Python algorithm (Appendix B) was implemented to visualize the depth of accumulated water, calculated as the difference between the generated runoff and the estimated maximum conveyance capacity for each sub-basin. The algorithm fills the DTM pixels starting from the lowest elevation and returns a water depth map. Finally, within the 3D scene, buildings positioned in flooded areas were highlighted with

different colors, based on the water level to which they are exposed.

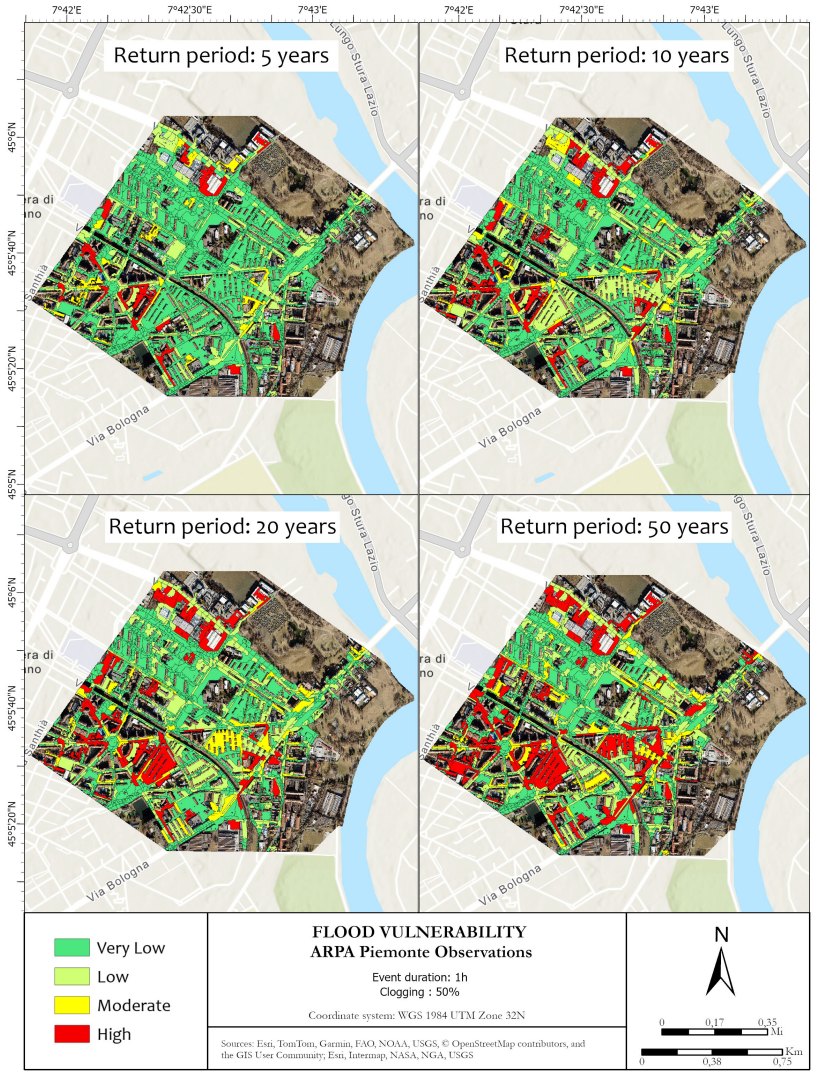

Figure 3.1: Flood vulnerability map: ARPA Piemonte observations (1994-2024) for 1 hour event duration and 50% clogging

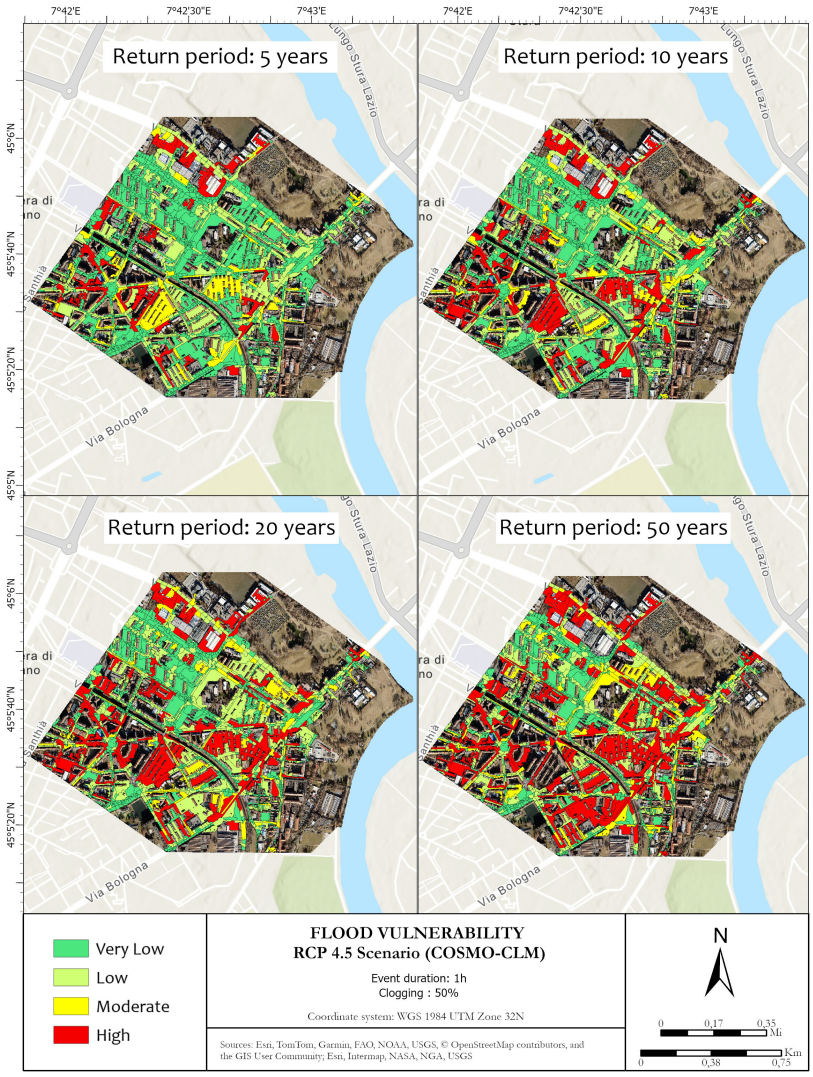

Figure 3.2: Flood vulnerability map: RCP 4.5 bias-corrected scenario (COSMO-CLM, 2026-2070) for 1 hour event duration and 50% clogging

Table 3.1: Quantitative distribution of sub-basins across vulnerability classes for different return periods and scenarios, considering 1-hour event duration and 50% clogging

Vulnerability class	Base scenario (observations)				Extreme scenario (RCP 4.5)			
	T=5	T=10	T=20	T=50	T=5	T=10	T=20	T=50
Very low (0-0.3)	1612	1520	1448	1344	1474	1349	1232	1103
Low (0.3-0.75)	178	248	289	351	274	351	420	471
Moderate (0.75-1)	20	26	70	58	43	54	66	90
High (>1)	18	34	71	75	37	74	110	164

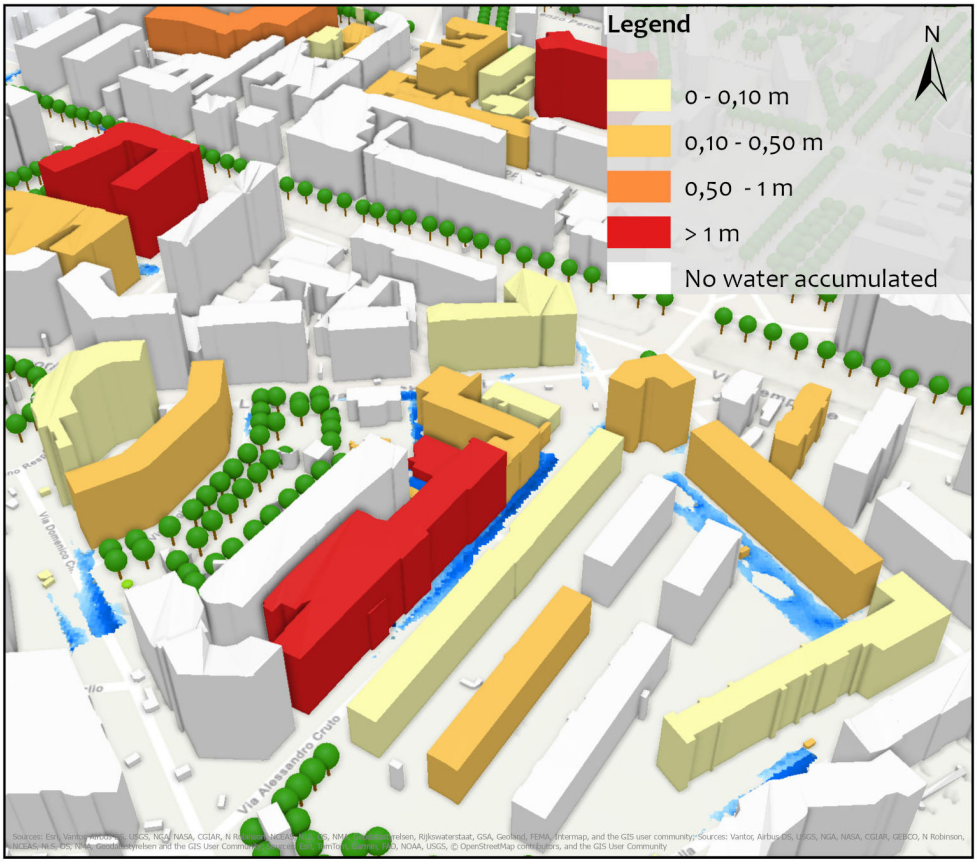

Figure 3.3: 3D model and visualization of exposed buildings to stormwater accumulation

Chapter 4

Discussion

4.1 Dataset Limitations and Assumptions

Although hourly rainfall data are more representative for urban flash floods, the limited temporal extent of the ARPA hourly time series did not ensure the statistical robustness necessary for IDF curve analysis. Therefore, daily data were used, with subsequent temporal disaggregation on an hourly scale. The resulting IDF curves were found to be consistent with the Atlas of Intense Rainfall in Piedmont by ARPA Piemonte, so the process was extended to future projections. Another limitation emerged during the acquisition of stormwater inlet positions. The latter were traced only along the main roads where street-level images were available, without making any distinction between type and size. Therefore, several areas remained unmapped, particularly private properties. To integrate the inlets dataset, a refinement was performed using Google Earth Pro, however many private areas remain inaccessible. It was chosen not to include any artificial nodes to ensure consistency of the data sources. However, this assumption led to two main consequences: the assignment of wide sub-basins to inlets positioned on the roads, or the lack of sub-basins in such areas. Therefore, it is possible that in some sub-basins there is a greater accumulation of water due to the absence of detected inlets. Despite this limitation, such spatial patterns provide a useful proxy to highlight regions requiring further data integration. Furthermore, the unavailability of detailed data on the urban drainage network, specifically the dimensions, materials, and slopes of the conduits, necessitated the adoption of simplified assumptions to quantify surface water ponding. The conveyance capacity of the underlying sewer pipes was identified as the primary hydraulic constraint of the system, using the standard design criteria mandated by the SMAT regulations as baseline reference parameters. Although this approximation may introduce uncertainties regarding the actual conveyance capacity, potentially leading to localized over- or under-estimations, the overall findings remain a robust indicator of how urban land use drives stormwater

accumulation. Ultimately, the assumption of a uniform 50% inlet clogging coefficient does not capture the dynamic nature of debris accumulation, representing a simplified worst-case scenario.

4.2 Methodological Assumptions and Modeling Uncertainties

Before the implementation of bias correction, a comparative analysis was conducted during the reference period 1979-2005 between ARPA rainfall observation and COSMO-CLM historical scenario, showing a MAE of 4.2 mm/day. Although high in absolute value, this parameter is indicative of the nature of the measurements. While the ARPA monitoring station records the local rainfall level at a specific location, the COSMO-CLM model returns an areal mean value along the grid cell (64 km^2). Consequently, precipitation events that affect the cell but do not directly affect the rain gauge were counted as errors in the MAE calculation. For the bias correction of future rainfall projections, the use of the QM method was assumed. As highlighted in the comparative review by Teutschbein & Seibert [21], it proved to be the most effective approach to correct simulated precipitation series during the reference period, ensuring a substantial improvement in the representation of the variance and distribution of extreme events compared to linear scaling methods. It is worth noting that the application of this technique implies the assumption of stationarity (i.e., that the systematic error of the model remains constant over time), a condition that cannot be guaranteed by considering future climate simulations. Nevertheless, the QM method was used to avoid underestimating annual precipitation maxima, which would otherwise have compromised the reliability of the flood simulations. For the calculation of the IDF curves, necessary for the simulation of precipitation scenarios, the RCP 4.5 scenario was considered from the COSMO-CLM model, since it presents precipitation intensities higher than the RCP 8.5 scenario for all return periods considered. A comparative analysis of the bias-corrected AMS during the period 2026–2070 also reveals this counterintuitive behavior of the scenarios. Despite the similarity in mean values, a substantial difference in variability was observed. In particular, the RCP 4.5 scenario shows a standard deviation ($\sigma = 32.81$ mm) greater than 30% the RCP 8.5 scenario ($\sigma = 24.45$ mm). This result explains the inversion of the IDF curves, indicating that the RCP 8.5 scenario tends to simulate a more uniform rainfall regime, despite being a worst-case scenario in terms of radiative forcing. Indeed, the analysis highlighted how the RCP 8.5 scenario is the wettest in terms of annual total precipitation and annual maximums.

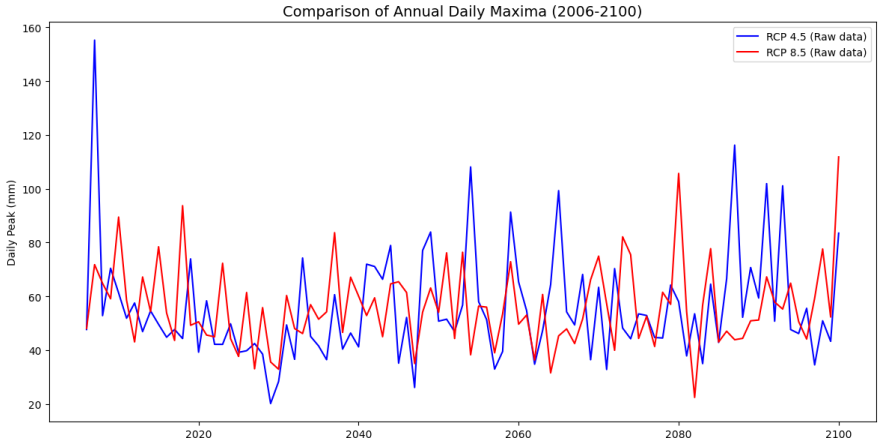

Figure 4.1: Comparison of annual daily maxima (RCP4.5 and RCP 8.5 raw time series)

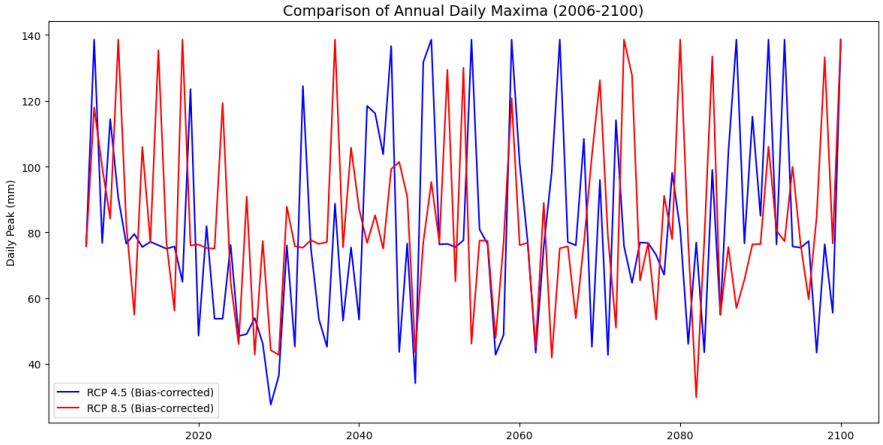

Figure 4.2: Comparison of annual daily maxima (RCP4.5 and RCP 8.5 bias-corrected time series)

The choice of the SCS-CN method to evaluate urban flood susceptibility is strongly supported by the recent literature. The SCS-CN model is widely recognized as one of the most reliable methods for estimating surface runoff, as it synthesizes complex environmental variables, such as soil characteristics, land use treatments, and topographical features, into a single CN parameter. As demonstrated by Shrestha et al. [2], coupling the SCS-CN model with a GIS environment provides a highly efficient approach that yields reliable results for the spatial runoff simulation. The validity of this empirical method is particularly evident in highly urbanized catchments, where the performance of the SCS-CN model is known to be highly

accurate for areas exhibiting a runoff coefficient greater than 0.5. The classification of HSG types was performed by comparing the equivalent hydraulic conductivity (K_z) values of the unsaturated zone, extracted from regional hydrogeological mapping, with the water transmission rate ranges defined by USDA standards. According to the TR-55 (USDA NRCS) manual, HSGs indicate the minimum infiltration rate obtained for bare soil after prolonged wetting. HSG also indicates the transmission rate at which the water moves within the soil; such a rate is controlled by the soil profile. K_z values were extracted from the Piedmont Geoportal, analytically calculated as the ratio between the total thickness of the unsaturated zone and the sum of the ratios between the thicknesses and conductivities of the individual lithological levels identified in approximately 2000 stratigraphies. Therefore, it is a parameter that describes the entire deep profile. Consequently, the choice to utilize K_z of the unsaturated zone is methodologically consistent with the definition of HSG, as it represents an integrated analytical measure of the water transport capacity through the entire stratigraphy of the subsoil. This approach allowed for overcoming the limitations of a classification based solely on surface texture (often altered in urban environments), ensuring an estimation of the infiltration and transmission potential within the hydrogeological configuration of the study area.

4.3 Interpretation of Rainfall Scenarios

The scenarios illustrated in Section 3 and Appendix A, for different return periods and event durations, show relevant findings for urban flood management. In all scenarios, it is evident how the drainage system, even considering the clogging factor of 50%, mitigates the runoff for events of lower intensity (3 or 6 hour events) and low return period (T=5 and T=10), keeping most of the sub-basins in the "Very low" vulnerability class. The number of sub-basins in the "High" vulnerability class increased significantly when considering a 50-year return period and a 1-hour event duration. By integrating climate projections into the maps, an amplification of flood vulnerability is shown, both in terms of the number of basins and the accumulation of water.

Also, some methodological assumptions to highlight the exposed buildings within the 3D model were introduced. A 2 m buffer was considered for each building, to which the maximum accumulated water value was assigned, previously estimated using a Python algorithm (Appendix B). Furthermore, the 3D model developed, as well as the ArcGIS algorithm for watershed delineation, does not take into account small-scale obstacles, but rather considers only DTM irregularities and buildings. In addition, to mitigate topographic anomalies, a geometric filter was introduced into the Python algorithm. Specifically, ponding depths exceeding

3 meters associated with negligible water volumes were flattened to the theoretical mean, thereby preventing the generation of unrealistic artifacts in the final map.

4.4 Challenges and Outlook

The integration of the SCS-CN method with GIS spatial analysis proved to be a robust approach for urban flood vulnerability assessment; however, several methodological challenges and assumptions must be acknowledged. Chief among these limitations is the simplification of the hydrodynamic processes. Specifically, the spatial routing of surface water in this study is based on a static volumetric accumulation algorithm. Although the applied Python-based approach identifies topographical depressions and calculates water depths, it neglects flow velocities and the temporal evolution of the flood event. Based on these findings, several promising opportunities emerge for future research. To overcome current limitations, future developments should focus on coupling the GIS-based SCS-CN outputs with a fully dynamic hydrodynamic model. Because the current static approach lacks a bidirectional link between the accumulated water on the surface and the sewer system, it cannot account for cross-basin water transfers. A transition to a dynamic model would allow for a comprehensive simulation of this dual-drainage system, capturing the complex interactions between pressurized sewer flows and overland water routing. Furthermore, a dynamic approach would provide crucial data on flow velocities and the temporal evolution of the flood event. Since peak discharge does not occur instantaneously but is governed by the catchment's time of concentration and specific lag time, capturing this timing is essential to determine the margin of intervention for emergency response. Based on these methodological improvements, transitioning from a 'vulnerability assessment' to a fully quantified 'flood risk and damage assessment' represents a crucial next step. As emphasized by Luino et al. [25], a comprehensive flood risk assessment requires specific data on the values of exposed assets, the degree of damage as a function of the event magnitude, and the attribution of an economic value to different exposed assets. By integrating the event simulation (water depths and velocities) with such socioeconomic vulnerability indicators and stage-damage curves, future studies could translate physical hazards into direct economic losses under different RCP scenarios. From a perspective of urban resilience, the high-vulnerability hotspots identified in this study provide potential targets for climate adaptation strategies. Future analyses should evaluate the mitigating impact of Nature-Based Solutions (NBS) and Sustainable Urban Drainage Systems (SUDS), such as permeable pavements, gardens, and green roofs, implemented within the critical sub-basins. Simulating the performance of these interventions under different RCP scenarios will be essential to ensure the long-term resilience of the city.

Chapter 5

Conclusions

This study evaluated flood vulnerability in the city of Turin, combining extreme rainfall scenarios, future projections, urban land use, and estimated drainage system conveyance capacity. The integration of the SCS-CN method with high-resolution LiDAR data in a GIS environment led to a framework for surface runoff simulation, considering several critical scenarios extracted from the IDF curves and introducing a stormwater inlets clogging factor of 50% to represent realistic operating conditions. Quantitative results showed the number of sub-basins vulnerable to water accumulation due to the excess of maximum inlet conveying capacity. The most critical areas fall into the "High" vulnerability class, with ponding depths ranging from a few centimeters to more than a meter. Worst-case scenarios are expected for a 50-year return period and a 1-hour event duration, where the increased intensity and rarity of the event generate the greatest amount of surface runoff. Climate projections allowed to visualize the potential urban flooding phenomenon in future scenarios. Due to increasing radiative forcing, the IDF curves for the previously bias-corrected RCP 4.5 and RCP 8.5 scenarios showed a greater intensity of events for all return periods and durations considered. From a methodological point of view, the Python-based approach with the application of a 2-meter buffer around the building footprints proved to be a highly effective GIS strategy. It estimated the accumulation of water on the surface due to overloading of the drainage network and visualized the most exposed buildings. The implemented workflow, although based on a static volumetric accumulation algorithm—thus neglecting the temporal evolution of the flood event and the cross-basin water transfer—represents a rapid and effective screening tool for urban planners. Furthermore, vulnerability maps constitute a first step towards proactive flood risk management, pinpointing the sub-basins where municipal efforts should be concentrated. By prioritizing the implementation of Nature-Based Solutions (NBS) and Sustainable Urban Drainage Systems (SUDS) in such critical areas, it would be possible to intercept and mitigate surface runoff, thus ensuring the long-term resilience of the Turin urban environment.

Appendix A

Flood Vulnerability Maps

Table A.1: Quantitative distribution of sub-basins across vulnerability classes for different return periods and scenarios, considering 1-hour event duration and 0% clogging

Vulnerability class	Base scenario (observations)				Extreme scenario (RCP 4.5)			
	T=5	T=10	T=20	T=50	T=5	T=10	T=20	T=50
Very low (0-0.3)	1766	1736	1697	1641	1709	1645	1568	1493
Low (0.3-0.75)	57	83	112	154	106	151	211	255
Moderate (0.75-1)	2	4	12	21	8	20	21	35
High (>1)	3	5	7	12	5	12	28	45

Table A.2: Quantitative distribution of sub-basins across vulnerability classes for different return periods and scenarios, considering 3-hour event duration and 0% clogging

Vulnerability class	Base scenario (observations)				Extreme scenario (RCP 4.5)			
	T=5	T=10	T=20	T=50	T=5	T=10	T=20	T=50
Very low (0-0.3)	1818	1802	1790	1777	1799	1777	1745	1696
Low (0.3-0.75)	10	25	36	45	28	45	74	113
Moderate (0.75-1)	0	1	2	5	1	5	5	11
High (>1)	0	0	0	1	0	1	4	8

Table A.3: Quantitative distribution of sub-basins across vulnerability classes for different return periods and scenarios, considering 3-hour event duration and 50% clogging

Vulnerability class	Base scenario (observations)				Extreme scenario (RCP 4.5)			
	T=5	T=10	T=20	T=50	T=5	T=10	T=20	T=50
Very low (0-0.3)	1759	1724	1682	1630	1704	1641	1578	1494
Low (0.3-0.75)	63	93	125	160	105	157	201	247
Moderate (0.75-1)	2	5	13	16	13	10	25	39
High (>1)	3	4	7	18	6	20	24	48

Table A.4: Quantitative distribution of sub-basins across vulnerability classes for different return periods and scenarios, considering 6-hour event duration and 0% clogging

Vulnerability class	Base scenario (observations)				Extreme scenario (RCP 4.5)			
	T=5	T=10	T=20	T=50	T=5	T=10	T=20	T=50
Very low (0-0.3)	1824	1819	1814	1806	1820	1809	1794	1771
Low (0.3-0.75)	4	7	11	20	8	19	31	52
Moderate (0.75-1)	0	0	0	0	0	0	2	2
High (>1)	0	0	0	0	0	0	0	3

Table A.5: Quantitative distribution of sub-basins across vulnerability classes for different return periods and scenarios, considering 6-hour event duration and 50% clogging

Vulnerability class	Base scenario (observations)				Extreme scenario (RCP 4.5)			
	T=5	T=10	T=20	T=50	T=5	T=10	T=20	T=50
Very low (0-0.3)	1801	1784	1767	1733	1777	1738	1694	1646
Low (0.3-0.75)	26	41	54	83	45	85	120	153
Moderate (0.75-1)	1	2	6	6	5	4	11	18
High (>1)	0	1	1	6	1	1	3	11

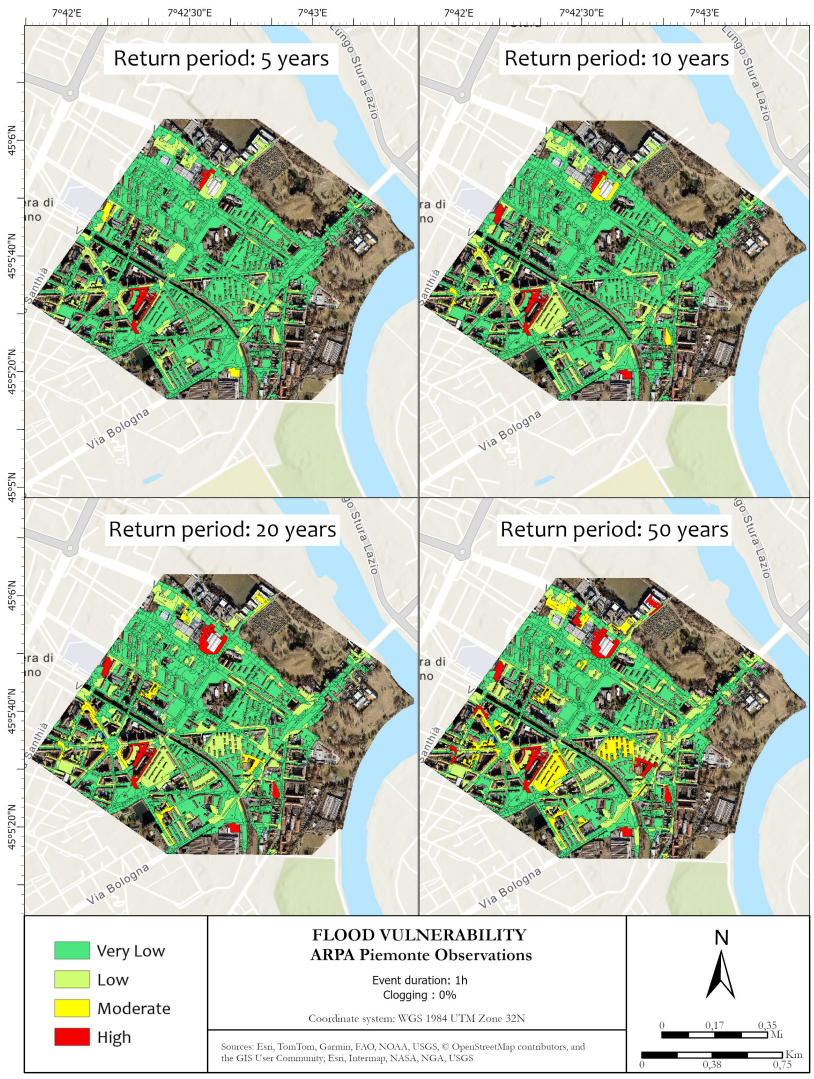

Figure A.1: Flood vulnerability map: ARPA Piemonte observations (1994-2024) for 1 hour event duration and 0% clogging

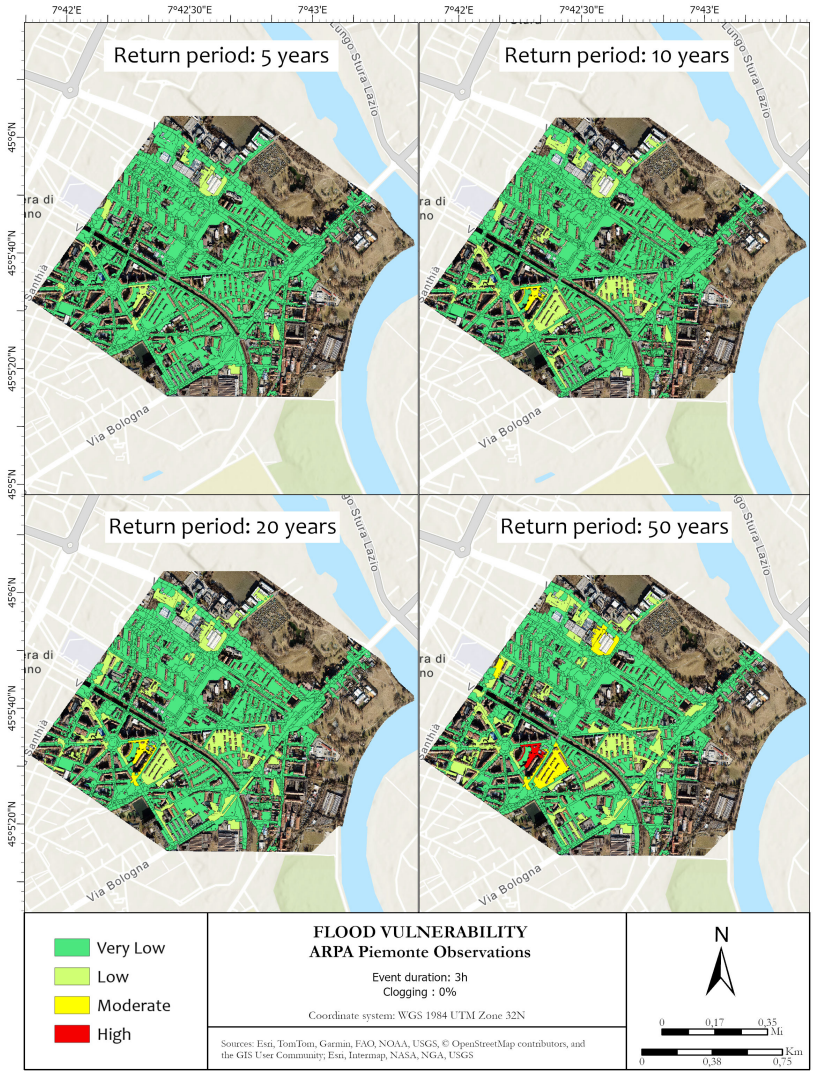

Figure A.2: Flood vulnerability map: ARPA Piemonte observations (1994-2024) for 3 hour event duration and 0% clogging

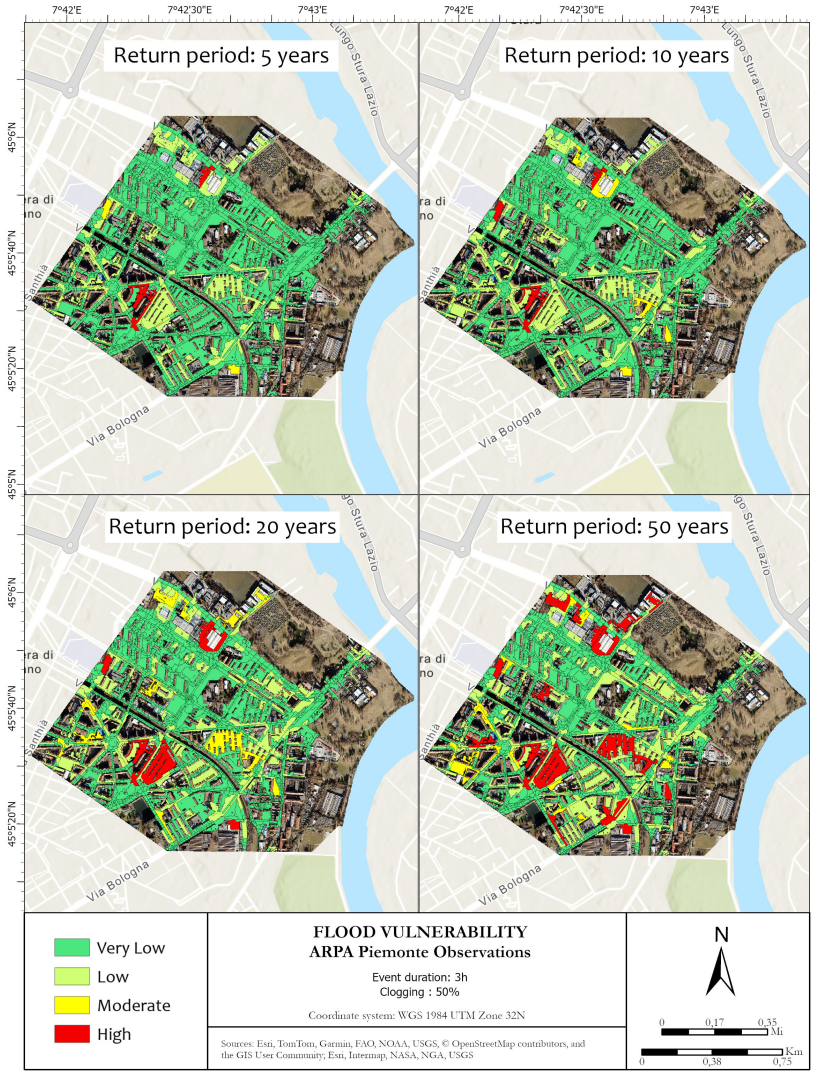

Figure A.3: Flood vulnerability map: ARPA Piemonte observations (1994-2024) for 3 hour event duration and 50% clogging

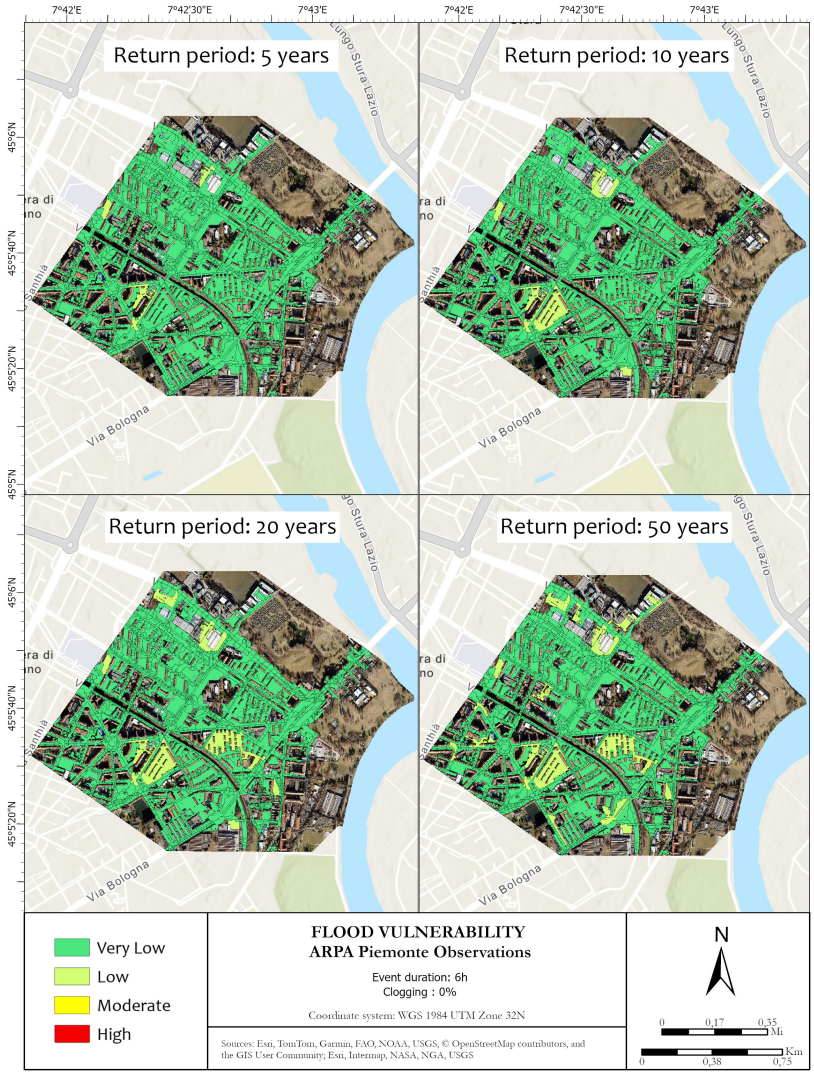

Figure A.4: Flood vulnerability map: ARPA Piemonte observations (1994-2024) for 6 hour event duration and 0% clogging

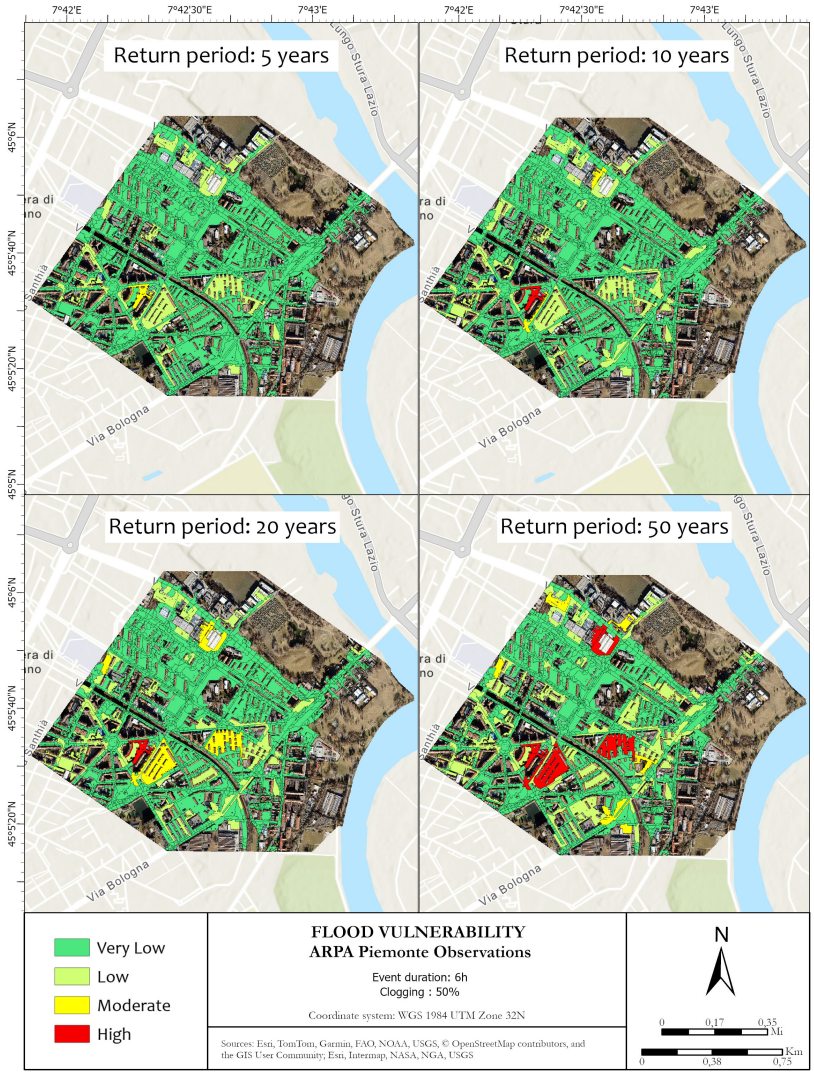

Figure A.5: Flood vulnerability map: ARPA Piemonte observations (1994-2024) for 6 hour event duration and 50% clogging

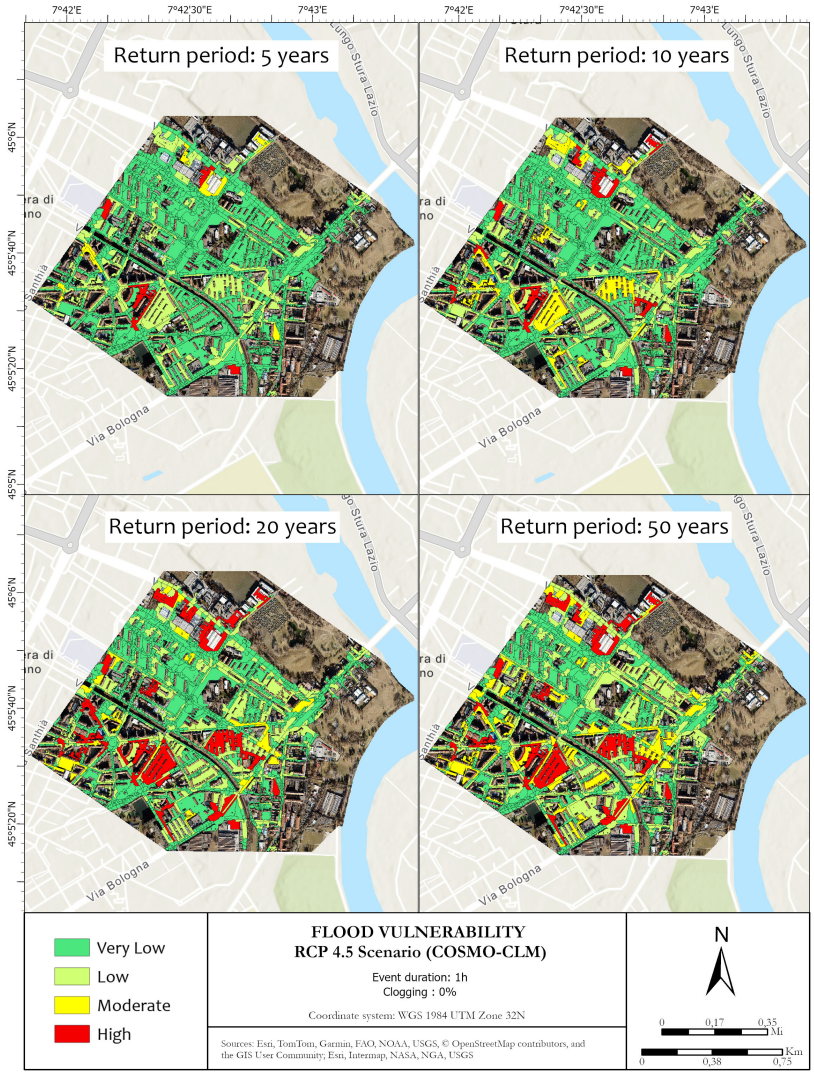

Figure A.6: Flood vulnerability map: RCP 4.5 bias-corrected scenario (COSMO-CLM, 2026-2070) for 1 hour event duration and 0% clogging

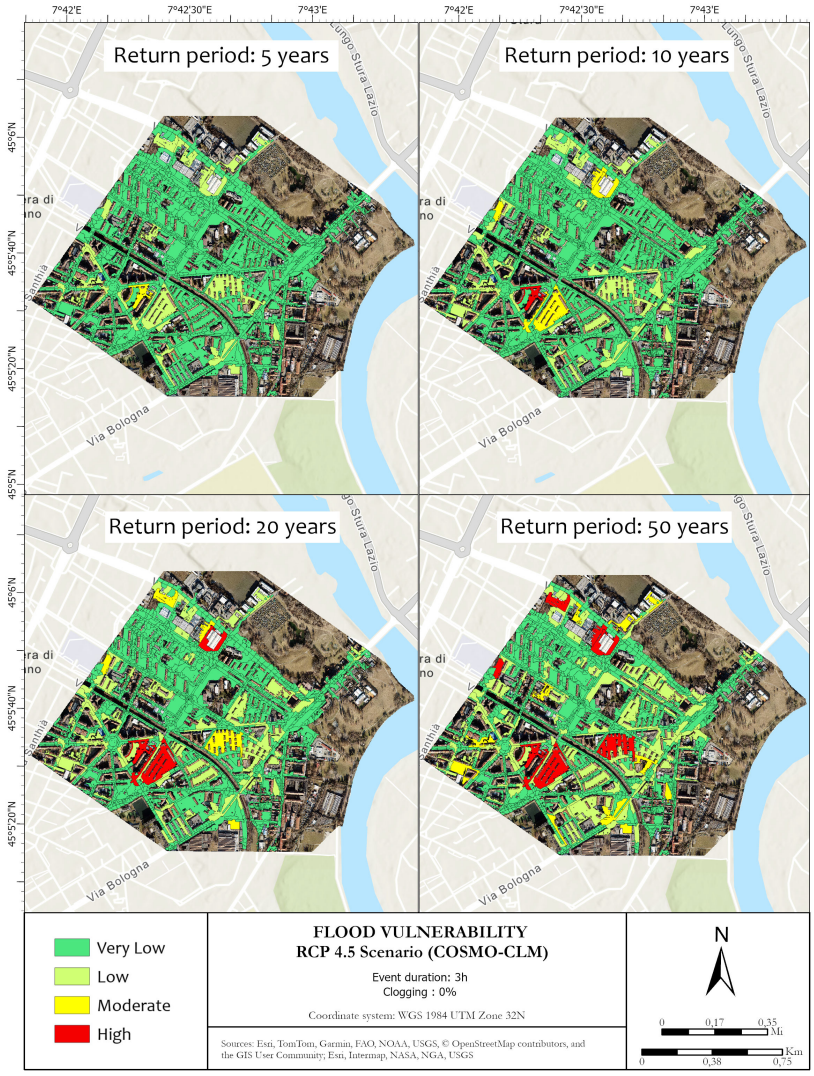

Figure A.7: Flood vulnerability map: RCP 4.5 bias-corrected scenario (COSMO-CLM, 2026-2070) for 3 hour event duration and 0% clogging

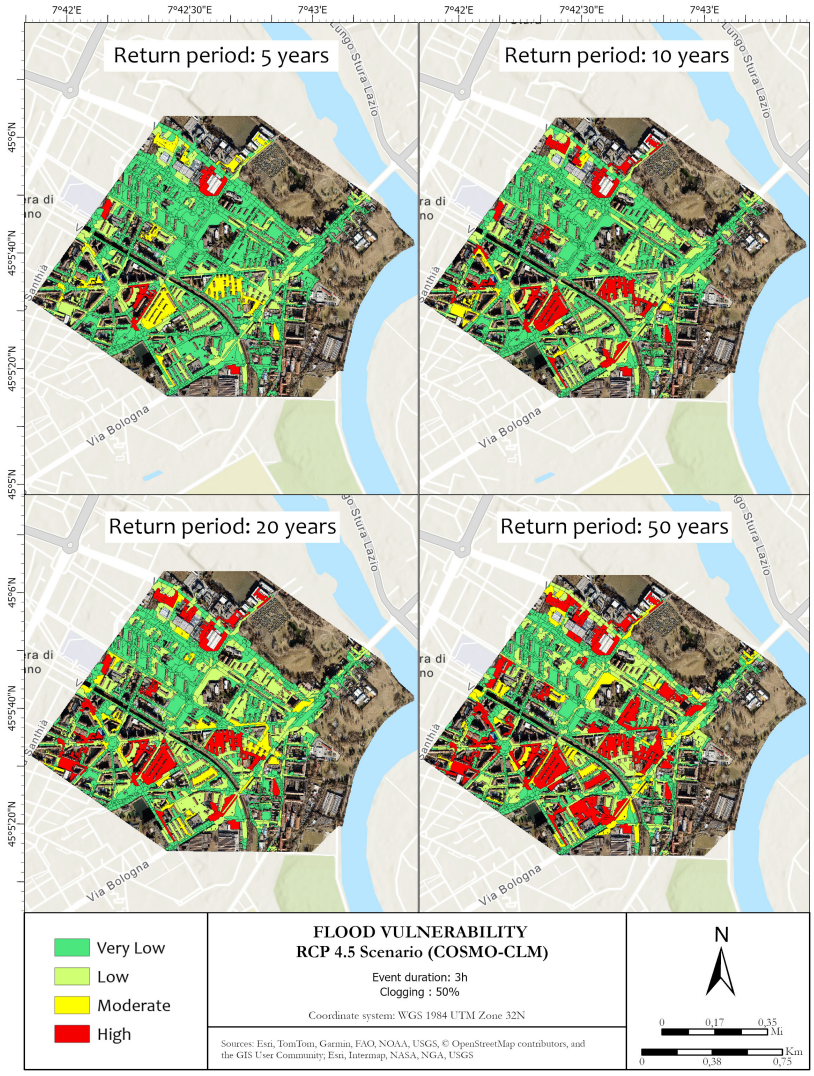

Figure A.8: Flood vulnerability map: RCP 4.5 bias-corrected scenario (COSMO-CLM, 2026-2070) for 3 hour event duration and 50% clogging

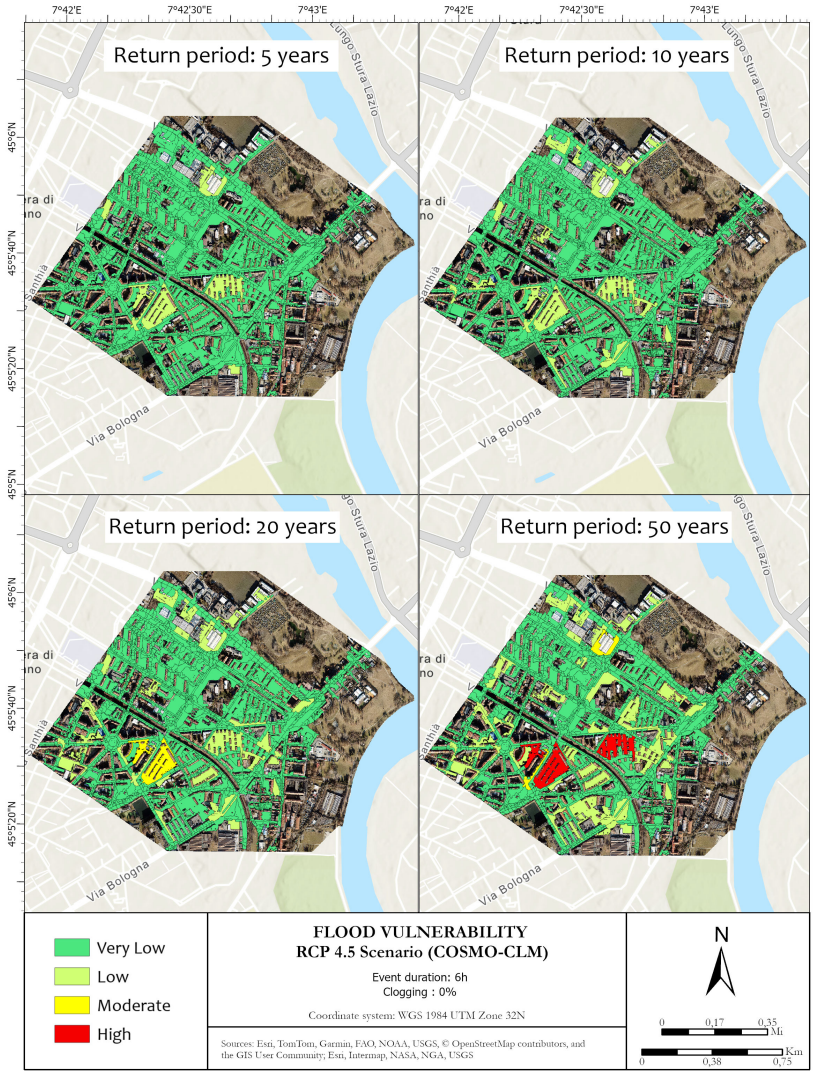

Figure A.9: Flood vulnerability map: RCP 4.5 bias-corrected scenario (COSMO-CLM, 2026-2070) for 6 hour event duration and 0% clogging

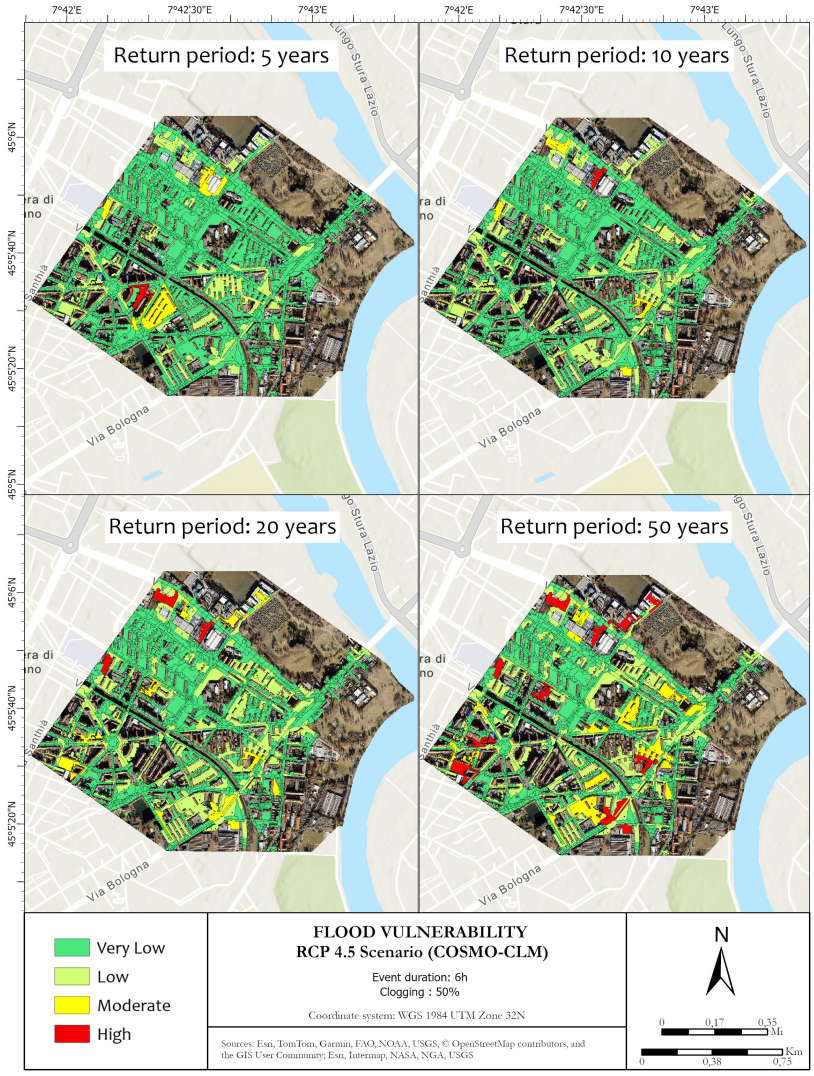

Figure A.10: Flood vulnerability map: RCP 4.5 bias-corrected scenario (COSMO-CLM, 2026-2070) for 6 hour event duration and 50% clogging

Appendix B

Water Accumulation Python Algorithm

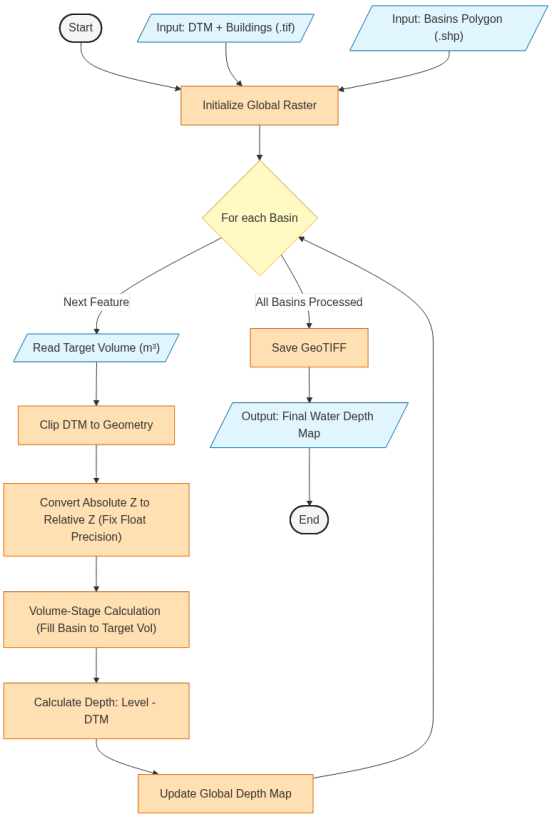

Figure B.1: Workflow for Python ponding algorithm

```
1
2  import rasterio
3  import rasterio.mask
4  import numpy as np
5  import pandas as pd
6  from rasterio.features import geometry_mask
7
8  # ==================== CONFIGURATION ====================
9  # Input paths (to be updated based on the local environment)
10
11 dtm_path = r"path/to/DTM.tif"
12 basins_path = r"path/to/basins.shp" #it contains a column of water
       volume in m^3
13 volume_column = "water_volume_m3"
14 output_raster = r"path/to/output/water_depth_map.tif"
15 # =======================================================
16
17 def get_water_level(dtm_array, target_volume_m3, cell_area,
     nodata_val):
18     """
19     Calculates the resulting water level allowing for ponding in
     local depressions.
20     To avoid numerical overflow errors, the calculation is
     performed using relative coordinates.
21     """
22     # Filter valid elevation values (excluding NoData)
23     valid_z = dtm_array[dtm_array != nodata_val]
24
25     if valid_z.size == 0 or target_volume_m3 <= 0:
26         return None
27
28     z_min = valid_z.min()
29
30     # --- THEORETICAL CHECK ---
31     total_area = valid_z.size * cell_area
32     theoretical_h = target_volume_m3 / total_area
33
34     # --- CRITICAL FIX: RELATIVE COORDINATES ---
35     # Working with relative elevations prevents significant
     numerical errors during cumulative sum operations.
36     valid_z_rel = valid_z - z_min
37     valid_z_rel = np.sort(valid_z_rel)
38
39     # --- PONDING ALGORITHM ---
40     # Float64 is strictly used to ensure maximum computational
     precision
41
```

```
    num_pixels = np.arange(1, len(valid_z_rel) + 1, dtype=np.float64)
    cumsum_z = np.cumsum(valid_z_rel, dtype=np.float64)

    # Available fillable volume for each elevation step
    volumes = ((valid_z_rel * num_pixels) - cumsum_z) * cell_area

    idx = np.searchsorted(volumes, target_volume_m3)

    if idx >= len(volumes):
        # Overflow Scenario:
        # The target volume exceeds the available depression storage.
        max_vol = volumes[-1]
        max_z_rel = valid_z_rel[-1]
        residual_vol = target_volume_m3 - max_vol
        top_area = len(valid_z_rel) * cell_area
        water_level_rel = max_z_rel + (residual_vol / top_area)
    else:
        # Normal Scenario:
        # The water volume is contained within the local depression.
        lower_vol = volumes[idx-1] if idx > 0 else 0
        wetted_area = idx * cell_area if idx > 0 else cell_area

        delta_vol = target_volume_m3 - lower_vol
        delta_h = delta_vol / wetted_area

        base_z_rel = valid_z_rel[idx-1] if idx > 0 else 0
        water_level_rel = base_z_rel + delta_h

    # --- SANITY CHECK ---
    # Exception handling for single-pixel sinks or anomalous extreme depths:
    # If the computed level is > 3m but the theoretical average is negligible (< 5cm), the depth is flattened to avoid artificial artifacts.
    if water_level_rel > 3.0 and theoretical_h < 0.05:
         return z_min + theoretical_h

    # Return to absolute elevation
    return z_min + water_level_rel

# --- EXECUTION ---
print("Reading input datasets...")
basins = gpd.read_file(basins_path)

with rasterio.open(dtm_path) as src:
    profile = src.profile
```

```
85      nodata = src.nodata
86      res = src.res
87      cell_area_m2 = res[0] * res[1]
88      full_shape = src.shape
89
90      final_depth_map = np.zeros(full_shape, dtype=np.float32)
91
92      print(f"Processing {len(basins)} sub-basins...")
93
94      for i, row in basins.iterrows():
95          vol = row[volume_column]
96          if vol <= 0 or pd.isna(vol): continue
97
98          geom = row.geometry
99          try:
100             # Mask the DTM using the current sub-basin geometry
101
102             masked_dtm, out_transform = rasterio.mask.mask(src, [
    geom], crop=True)
103             masked_dtm = masked_dtm[0]
104         except ValueError:
105             # Skip if the geometry does not overlap the raster
    extent
106             continue
107
108         w_level = get_water_level(masked_dtm, vol, cell_area_m2,
    nodata)
109
110         if w_level is not None:
111             # Calculate local water depth
112             local_depth = w_level - masked_dtm
113             local_depth[masked_dtm == nodata] = 0
114             local_depth[local_depth < 0] = 0
115
116             # Write results back to the master array
117             minx, miny, maxx, maxy = geom.bounds
118             row_start, col_start = src.index(minx, maxy)
119             r_end = min(row_start + local_depth.shape[0],
    full_shape[0])
120             c_end = min(col_start + local_depth.shape[1],
    full_shape[1])
121             h_local = r_end - row_start
122             w_local = c_end - col_start
123
124             if h_local > 0 and w_local > 0:
125                 current_slice = final_depth_map[row_start:r_end,
    col_start:c_end]
126                 new_vals = local_depth[:h_local, :w_local]
127                 mask_water = new_vals > 0
```

```
128                 # Retain the maximum water depth if overlaps occur
129                 current_slice[mask_water] = np.maximum(
    current_slice[mask_water], new_vals[mask_water])
130                 final_depth_map[row_start:r_end, col_start:c_end]
    = current_slice
131
132     # --- EXPORT RESULTS ---
133     print(f"Saving output raster to: {output_raster}")
134     # Update profile parameters (NoData set to 0 for visualization
    )
135     profile.update(dtype=rasterio.float32, count=1, compress='lzw'
    , nodata=0)
136
137     with rasterio.open(output_raster, 'w', **profile) as dst:
138         dst.write(final_depth_map, 1)
139
140 print("Processing complete. Ponding depth map generated
    successfully.")
```

Listing B.1: Python ponding algorithm

Bibliography

[1] A. K. Jha, R. Bloch, and J. Lamond. *Cities and Flooding: A Guide to Integrated Urban Flood Risk Management for the 21st Century*. Tech. rep. © World Bank. License: CC BY 3.0 IGO. Washington, DC: World Bank, 2012. URL: http://hdl.handle.net/10986/2241 (cit. on p. 1).

[2] Sabita Shrestha, Shenghui Cui, Lilai Xu, Lihong Wang, Bikram Manandhar, and Shengping Ding. «Impact of Land Use Change Due to Urbanisation on Surface Runoff Using GIS-Based SCS–CN Method: A Case Study of Xiamen City, China». In: *Land* 10.8 (2021), p. 839. DOI: 10.3390/land10080839 (cit. on pp. 2, 38).

[3] Maria Gabriella Forno, Franco Gianotti, and Umberto Storti. «Geomorphology of the Po Fluvial Terraces in Turin Deduced by New Subsoil Data (NW Italy)». In: *Water* 14.18 (2022), p. 2872. DOI: 10.3390/w14182872 (cit. on p. 3).

[4] Esri. *World Imagery Basemap*. Esri, HERE, Garmin, © OpenStreetMap contributors, and the GIS user community. 2025. URL: https://server.arcgisonline.com/arcgis/rest/services/World_Imagery/MapServer (cit. on p. 4).

[5] GADM. *Database of Global Administrative Areas, Version 4.1*. 2022. URL: http://www.gadm.org (cit. on p. 4).

[6] Città di Torino. *Geoportale e Governo del Territorio - CTC*. 2024. URL: http://geoportale.comune.torino.it/web/ (cit. on p. 6).

[7] Digitarca s.r.l. *SmartCity3D*. 2025. URL: https://www.smartcity3d.com/ (cit. on p. 6).

[8] ARPA Piemonte. *Agenzia Regionale per la Protezione Ambientale del Piemonte*. 2024. URL: https://www.arpa.piemonte.it/ (cit. on p. 6).

[9] B. Rockel, A. Will, and A. Hense. «The regional climate model COSMO-CLM (CCLM)». In: *Meteorologische Zeitschrift* 17.4 (2008), pp. 347–348 (cit. on pp. 6, 26).

[10] E. Bucchignani, M. Montesarchio, A. L. Zollo, and P. Mercogliano. «High resolution climate simulations with COSMO-CLM over Italy: performance evaluation and climate projections for the 21st century». In: *International Journal of Climatology* 36.2 (2015), pp. 735–756. DOI: 10.1002/joc.4379 (cit. on pp. 6, 26).

[11] A. L. Zollo, V. Rillo, E. Bucchignani, M. Montesarchio, and P. Mercogliano. «Extreme temperature and precipitation events over Italy: assessment of high resolution simulations with COSMO-CLM and future scenarios». In: *International Journal of Climatology* 36.2 (2015), pp. 987–1004. DOI: 10.1002/joc.4401 (cit. on pp. 6, 26).

[12] American Society for Photogrammetry and Remote Sensing. *ASPRS Positional Accuracy Standards for Digital Geospatial Data*. Tech. rep. ASPRS, 2024. URL: https://asprs.org/Main/Main/Standards/Positional-Accuracy-Standards.aspx (cit. on pp. 8, 9).

[13] Joachim Höhle and Michael Höhle. «Accuracy assessment of digital elevation models by means of robust statistical methods». In: *ISPRS Journal of Photogrammetry and Remote Sensing* 64.4 (2009), pp. 398–406. DOI: 10.1016/j.isprsjprs.2009.02.003 (cit. on p. 9).

[14] SMAT S.p.A. *Regolamento del Servizio Idrico Integrato*. Società Metropolitana Acque Torino S.p.A. Torino, 2018 (cit. on p. 17).

[15] Oppo. *Calcolo portata di una condotta circolare a pelo libero*. 2025. URL: https://www.oppo.it/calcoli/canali/portatacanale2.html (cit. on p. 18).

[16] Ven Te Chow, David R. Maidment, and Larry W. Mays. *Applied Hydrology*. McGraw-Hill International Editions, 1988 (cit. on pp. 19, 23, 24, 29).

[17] The SciPy community. *SciPy API Reference: scipy.stats.anderson*. 2024. URL: https://docs.scipy.org/doc/scipy/reference/generated/scipy.stats.anderson.html (cit. on p. 21).

[18] D. N. Moriasi, J. G. Arnold, M. W. Van Liew, R. L. Bingner, R. D. Harmel, and T. L. Veith. «Model Evaluation Guidelines for Systematic Quantification of Accuracy in Watershed Simulations». In: *Transactions of the ASABE* 50.3 (2007), pp. 885–900. DOI: 10.13031/2013.23153 (cit. on p. 22).

[19] ARPA Piemonte. *Le Precipitazioni Intense del Piemonte. Distribuzione regionale delle piogge e caratterizzazione statistica dei valori estremi*. Tech. rep. Agenzia Regionale per la Protezione Ambientale del Piemonte, 2013 (cit. on p. 23).

[20] ARPA Piemonte. *Atlante delle Piogge - Dati di precipitazione estrema*. https://webgis.arpa.piemonte.it/atlante_pioggia_webapp/grafici_new/index_gev.php?NUMCODICE=191454. 2024 (cit. on p. 24).

[21] Claudia Teutschbein and Jan Seibert. «Bias correction of regional climate model simulations for hydrological climate-change impact studies: Review and evaluation of different methods». In: *Journal of Hydrology* 456–457 (2012), pp. 12–29. DOI: 10.1016/j.jhydrol.2012.05.052 (cit. on pp. 26, 37).

[22] Mathieu Vrac, Harilaos Loukos, Thomas Noël, and Dimitri Defrance. «Should We Use Quantile-Mapping-Based Methods in a Climate Change Context? A "Perfect Model" Experiment». In: *Climate* 13.7 (2025), p. 137. DOI: 10.3390/cli13070137 (cit. on p. 26).

[23] USDA NRCS. *Urban Hydrology for Small Watersheds*. Tech. rep. Technical Release 55 (TR-55). United States Department of Agriculture, Natural Resources Conservation Service, 1986 (cit. on pp. 29, 31).

[24] Regione Piemonte. *Geoportale Piemonte - Infrastruttura Geografica Regionale*. https://geoportale.igr.piemonte.it/cms/. 2025 (cit. on p. 30).

[25] F. Luino, M. Chiarle, G. Nigrelli, A. Agangi, M. Biddoccu, C. G. Cirio, and W. Giulietto. «A model for estimating flood damage in Italy: preliminary results». In: *WIT Transactions on Ecology and the Environment* 98 (2006), pp. 101–112. DOI: 10.2495/EEIA060071 (cit. on p. 40).